Title: Tumor cell heterogeneity drives spatial organization of the intratumoral immune response in squamous cell skin carcinoma

Authors:

Miho Tanaka[1], Lotus Lum[1], Kenneth Hu[2], Cecilia Ledezma-Soto[1], Bushra Samad[2], Daphne Superville[1], Kenneth Ng[1], Zoe Adams[1], Kelly Kersten[3], Lawrence Fong[4,5], Alexis J. Combes[2,5,6], Matthew Krummel[3,5], Melissa Reeves[7,8]

Affiliations:

[1]Department of Microbiology and Immunology, University of California San Francisco, San Francisco, CA, USA.

[2]UCSF CoLabs, University of California San Francisco, San Francisco, CA, USA.

[3]Department of Pathology, University of California San Francisco, San Francisco, CA, USA.

[4]Division of Hematology and Oncology, Department of Medicine, University of California San Francisco, San Francisco, CA, USA.

[5]ImmunoX Initiative, University of California San Francisco, San Francisco, CA, USA.

[6]Division of Gastroenterology, Department of Medicine, University of California San Francisco, San Francisco, CA, USA.

[7]Huntsman Cancer Institute, University of Utah, Salt Lake City, UT, USA.

[8]Department of Pathology, University of Utah, Salt Lake City, UT, USA.

Keywords:

Intratumoral heterogeneity, tumor immune microenvironment, immune checkpoint blockade, spatial immune heterogeneity

Abstract:

Intratumoral heterogeneity (ITH)—defined as genetic and cellular diversity within a tumor—is linked to failure of immunotherapy and an inferior anti-tumor immune response. The underlying mechanism of this association is unknown. To address this question, we modeled heterogeneous tumors comprised of a pro-inflammatory ("hot") and an immunosuppressive ("cold") tumor population, labeled with YFP and RFP tags respectively to enable precise spatial tracking. The resulting mixed-population tumors exhibited distinct regions comprised of YFP^+ (hot) cells, RFP^+ (cold) cells, or a mixture. We found that tumor regions occupied by hot tumor cells (YFP^+) harbored more total T cells and a higher frequency of Th1 cells and $IFN\gamma^+$ CD8 T cells compared to regions occupied by cold tumor cells (RFP^+), whereas immunosuppressive macrophages showed the opposite spatial pattern. We identified the chemokine CX3CL1, produced at higher levels by our cold tumors, as a mediator of intratumoral macrophage accumulation, particularly immunosuppressive $CD206^{Hi}$ macrophages. Furthermore, we examined the response of heterogeneous tumors to a therapeutic combination of PD-1 blockade and CD40 agonist on a region-by-region basis. While the combination successfully increases Th1 abundance in "cold" tumor regions, it fails to bring overall T cell activity to the same level as seen in "hot" regions. The presence of the "cold" cells thus ultimately leads to a failure of the therapy to induce tumor rejection. Collectively, our results demonstrate that the organization of heterogeneous tumor cells has a profound impact on directing the spatial

45 organization and function of tumor-infiltrating immune cells as well as on responses to
46 immunotherapy.
47
48
49 **Introduction:**
50 Immunotherapies have shown great promise in treating cancer by activating a patient's
51 own immune cells to fight their tumor, but only a fraction of patients respond to current
52 treatment regimens[1–4]. Immune checkpoint blockade (ICB) therapy routinely achieves durable
53 cures in only a limited number of cancer types, and in many tumor types, response rates are as
54 low as 15% with high relapse rates[3,4]. Genetic heterogeneity within a tumor is a significant
55 factor that has been linked to poor ICB response[5–7]. Tumors are often comprised of multiple
56 populations of cancer cells, with each population carrying a distinct set of genetic alterations
57 and phenotypic behaviors[8–10]. Genetic heterogeneity—often given the generalized label
58 "intratumoral heterogeneity" (ITH)—is inherent in all cancer types[6], and studies in multiple
59 cancer types have shown that tumors with high genetic heterogeneity (high ITH) are less likely
60 to respond to ICB regimens[5,7]. Further, in patients, tumors are frequently a patchwork of "hot"
61 and "cold" regions[11–13]—characterized by high and low T cell infiltrates, respectively —
62 indicating that a dysfunctional T cell phenotype can be spatially localized[14]. One study of 85 pre-
63 treatment lung cancers revealed that over two-thirds of tumors investigated contained both
64 hot and cold regions[11]. However, model systems that lend themselves to mechanistically
65 interrogating the impact of tumor heterogeneity on the spatial organization of immune cells
66 within a tumor are limited at present.

67 Heterogeneity-induced impairment of the anti-tumor immune response has also been
68 observed in mouse models[15–17]. A mixture of two mouse pancreatic ductal adenocarcinoma
69 (PDAC) cell lines, one giving rise to immune hot and the other to immune cold tumors on its
70 own, resulted in an overall cold tumor, suggesting that coldness may be a dominant
71 phenotype[15]. Another study in a murine melanoma model showed that high-heterogeneity
72 tumors exhibited an inferior CD8 T cell response compared to low-heterogeneity tumors[16].
73 Building on this, we set out to ask not only how tumor heterogeneity impacts the immune
74 response in the tumor as a whole, but also to interrogate its impact on the spatial organization
75 of the intratumoral immune response.
76 Our studies employed tumor cell lines derived from carcinogen-induced squamous cell
77 skin carcinomas, induced by dimethylbenzanthracene and 12-O-tetradecanoylphorbol-13-
78 acetate (DMBA/TPA)[18,19]. The DMBA/TPA skin carcinogenesis model gives rise to tumors that
79 exhibit a physiologically relevant range of mutational burdens[20,21] and develop in immune-
80 competent hosts, resulting in tumors with neoantigen and immune profiles that mimic those
81 found in human tumors. We have generated cell lines from DMBA/TPA-induced tumors, which,
82 when implanted into mice, give rise to tumors with reproducible immune phenotypes. Here, we
83 develop a novel model of heterogeneous tumors by implanting a mixture of two such cell lines.
84 Each cell line, labeled with a fluorophore, represents a distinct, trackable population within the
85 tumor. The two cell lines we selected share a common oncogenic driver, *Hras* Q61L, but also
86 each contain over 100 distinct nonsynonymous mutations; their combination thus models a
87 genetically heterogeneous tumor.

88 Using this novel model system, we here interrogate the mechanisms by which
89 heterogeneity in tumor cells impacts the immune response, the spatial organization of
90 infiltrating immune cells, and the response to ICB therapy. We find, not surprisingly, that the
91 cold tumor population drives an overall cold immune phenotype at a whole tumor level.
92 Further, we observe that our constituent tumor populations form a patchwork pattern within
93 the tumor. Our study reveals that the spatial organization of the tumor cells themselves creates
94 an architectural blueprint that dictates the spatial localization and function of infiltrating
95 immune cells. We observe T cells preferentially accumulating and exhibiting superior effector
96 function in the neighborhood of hot tumor cells, while cold tumor cells recruit an
97 immunosuppressive microenvironment to their immediate vicinity. The presence of the cold
98 tumor cells further mediates resistance to ICB therapy in mixed-population tumors. However,
99 to our surprise, we observe that immunotherapy successfully improves the quality of the
100 immune response in cold tumor regions—but not to a sufficient degree to induce robust tumor
101 regression. Our model system of heterogeneity thus illuminates how heterogeneity in tumor
102 cells impacts both the endogenous anti-tumor immune response and the efficacy of therapy on
103 a highly localized spatial scale.
104
105 **Results:**
106
107 **Modeling heterogeneous tumors with trackable tumor populations.**
108 We have established a series of squamous cell skin carcinoma cell lines, named the CIT
109 ("carcinogen-induced tumor") lines, derived from DMBA/TPA-induced skin carcinomas that

110 were initiated in *K5-CreER^{T2}-Confetti* mice on an FVB background[19]. To establish a model system
111 in which to study the impact of tumor heterogeneity on the immune response, we selected and
112 combined two of these cell lines, CIT6 and CIT9, that give rise respectively to tumors exhibiting
113 a high and low frequency of overall T cells, CD4 T cells and CD8 T cells, representing
114 immunologically hot and cold tumors. We introduced fluorescent labels into these tumor cells,
115 taking advantage of CIT lines originating from mice carrying an unactivated *Confetti* cassette.
116 We treated CIT6 and CIT9 with adenoviral Cre recombinase (AdCre), leading to recombination
117 of the *Confetti* allele and stochastic labeling of each cell with one of four fluorescent proteins—
118 yellow, red, cyan and green fluorescent protein (YFP, RFP, CFP and GFP, respectively)[22]. We
119 then sorted YFP$^+$ cells from the CIT6 line and RFP$^+$ cells from the CIT9 line to establish
120 fluorescently-tagged CIT6-YFP and CIT9-RFP cell lines. For all subsequent experiments, these
121 fluorescently labeled cell lines were implanted into syngeneic *Confetti* mice, carrying an
122 unactivated *Confetti* allele, which recapitulated the expected hot and cold immune phenotypes
123 we observed when unlabeled CIT6 and CIT9 tumor cells were implanted into wild-type FVB mice
124 (**Fig. 1A-D**; Supp Fig. 1).
125 To model heterogeneous tumors, we injected mice subcutaneously with an equal
126 mixture of CIT6-YFP and CIT9-RFP cell lines (6.25×10^4 cells each, totaling 1.25×10^5 cells per
127 injection) (**Fig. 1E**). Tumors were assessed for composition by fluorescent stereomicroscope at
128 the time of harvest, when tumors were 1cm in longest diameter (21-28 days). We consistently
129 observed approximately 2/3 of the resulting tumors were comprised of both YFP$^+$ and RFP$^+$ cells
130 with clearly defined YFP$^+$ and RFP$^+$ regions, whereas the remaining 1/3 consisted of only RFP$^+$
131 cells in most cases, or only YFP$^+$ cells in rare cases (**Fig. 1F**, data not shown). The tumors that

132 contained both YFP$^+$ and RFP$^+$ cells, termed “mixed-population tumors” herein, were used for
133 downstream analyses. When the equal mixture of CIT6-YFP and CIT9-RFP cells was implanted
134 into immunodeficient NOD/SCID/IL-2Rɣ null (NSG) mice, which lack T, B and NK cells and innate
135 lymphoid cells (ILCs), we observed a higher penetrance of mixed-population tumors, indicating
136 that immune activity against tumor cells was likely responsible for cases where mixed tumors
137 failed to establish (Supp Fig. 2). Inspection of the mixed-population tumors by cryosectioning
138 and fluorescent imaging showed a patchwork of regions that could be classified as being
139 occupied primarily by YFP$^+$ cells, primarily by RFP$^+$ cells, or by a mixture of both populations
140 (**Fig. 1G**). The fluorescent tags in these cell lines thus successfully enabled spatial tracking and
141 quantification of each tumor population in the mixed-tumor population tumors and enabled us
142 to establish a novel model to study ITH.
143
144 **An immunosuppressive phenotype dominates the immune microenvironment of mixed-**
145 **population tumors.**
146 To determine how each constituent tumor population affects the overall immune
147 response in mixed-population tumors, we performed a comprehensive flow cytometric analysis
148 of the immune infiltrates (Supp Fig. 3) found in CIT6-YFP + CIT9-RFP mixed-population tumors
149 and compared this to infiltrates found in each CIT6-YFP and CIT9-RFP single-population tumors.
150 Mixed-population tumors have an overall cold immune phenotype, exhibiting CD4 and CD8 T
151 cell infiltration comparable to CIT9-RFP tumors and significantly lower than that found in CIT6-
152 YFP tumors (**Fig. 2A**). MHC-I proteins were expressed on more than 85% of CIT6-YFP and CIT9-
153 RFP tumor cells and expressed at a similar level (**Fig. 2B**), suggesting that the differences in T

154 cell abundance are not due to the differences in MHC-I expression. MHC-II expression was very
155 low on both CIT6-YFP and CIT9-RFP tumor cells (Supp. Fig. 4A), in line with these tumors being
156 of epithelial origin. Although there was no significant difference in the fraction of CD4 T cells
157 that were regulatory T cells (Tregs; $CD4^+$ $CD25^+$ $Foxp3^+$) or in the CD8 T cell-to-Treg ratio
158 between any of the groups, CIT9-RFP and mixed-population tumors showed a lower CD4 Teff
159 ($CD4^+$ $CD25^-$ $Foxp3^-$)-to-Treg cell ratio than CIT6-YFP tumors, suggesting a skewing in CIT9-RFP
160 and mixed tumors toward an immunosuppressive microenvironment (**Fig. 2C**). Other
161 lymphocytes, specifically B cells and $NKp46^+$ lymphocytes (including natural killer (NK) cells and
162 innate lymphoid cells (ILCs)), showed a similar pattern: CIT6-YFP tumors showed significantly
163 higher infiltration by both lymphoid populations than CIT9-RFP tumors, and mixed-population
164 tumors overall resembled CIT9-RFP tumors (although the difference between $NKp46^+$
165 lymphocytes in CIT6-YFP versus mixed tumors was not statistically significant) (**Fig. 2D**). By
166 contrast, CIT9-RFP tumors showed a higher infiltration than CIT6-YFP tumors of $F4/80^+$ $CD11b^+$
167 MHC-II^+ macrophages (**Fig. 2E**) and $CD11b^+$ myeloid cells (Supp Fig. 4B), which often harbor
168 immunosuppressive properties in the tumor microenvironment[23,24]. Mixed-population tumors
169 also had an increase in $CD11b^+$ myeloid cells and a trend toward more macrophages compared
170 to CIT6-YFP tumors, again exhibiting more similarity in immune profile to CIT9-RFP tumors (**Fig.**
171 **2E,** Supp Fig. 4B). $Ly6G^+$ $Ly6C^{mid}$ neutrophils, $Ly6G^-$ $Ly6C^+$ monocytes, and $CD11b^+$ $CD11c^+$ MHC-
172 II^+ $F4/80^-$ dendritic cells (DCs), which are conventionally anti-tumoral effector cells, all showed a
173 trend toward lower frequency in both CIT9-RFP and mixed tumors compared to CIT6-YFP
174 tumors, albeit not statistically significant differences (Supp Fig. 4C). Collectively, these data
175 support our designation of CIT6-YFP tumors as pro-inflammatory and immune hot, and of CIT9-

176 RFP tumors as immunosuppressive and immune cold, and further reveal that the
177 immunosuppressive phenotype is dominant in mixed-population tumors.
178 Macrophages are conventionally known to facilitate antigen presentation and assist in T
179 cell activation, but in the context of a tumor, evidence suggests that tumor-associated
180 macrophages (TAMs) are more frequently a mediator of immunosuppression[24]. TAMs are the
181 most abundant immune cells in CIT6-YFP and CIT9-RFP tumors, comprising 30-80% of total
182 $CD45^+$ immune cells. Therefore, we sought to determine if $F4/80^+$ $CD11b^+$ $MHC\text{-}II^+$ macrophages
183 in our tumors are functionally immunosuppressive. Macrophages were sorted from CIT6-YFP,
184 CIT9-RFP, and mixed-population tumors, and assessed for their capacity to suppress CD8 T cells
185 isolated from naïve, non-tumor bearing syngeneic *Confetti* mice and activated by CD3/CD28
186 beads. In comparison to CD8 T cells alone, the addition of TAMs significantly suppressed CD8 T
187 cell proliferation, measured as the number of cells that had undergone division (as marked by
188 CFSE dilution) (**Fig. 2F**). The expansion of activated T cells, measured as $CD69^+$ $CD25^+$ $CD8^+$ T
189 cells (early activation), $CD69^-$ $CD25^+$ $CD8^+$ T cells (late activation), or $PD\text{-}1^+$ $CD8^+$ T cells, showed
190 similar results, with the addition of macrophages decreasing the number of activated T cells
191 (**Fig. 2G**, Supp Fig. 4D). Moreover, the expansion of the $CD62L^-$ $CD44^+$ effector T cell subset and
192 the $CD62L^+$ $CD44^+$ central memory T cell subset was significantly suppressed in the presence of
193 TAMs (**Fig. 2H**, Supp Fig. 4E). Surprisingly, no difference in immunosuppressive capacity was
194 observed between TAMs derived from CIT6-YFP, CIT9-RFP or mixed-population tumors (**Fig. 2F-**
195 **H**). Thus, macrophages in CIT6-YFP, CIT9-RFP and mixed-population tumors are equally
196 immunosuppressive, but we conclude that the increased abundance of these macrophages in

197 CIT9-RFP and mixed-population tumors **(Fig. 2E)** may be responsible for creating a more
198 suppressive immune microenvironment in those tumors.
199
200 **Spatial organization of tumor populations drives the spatial organization of immune cells.**
201 Since the mixed-population tumors were comprised of a patchwork of YFP, mixed, and
202 RFP tumor regions, we next sought to better understand whether the "dominant cold" immune
203 phenotype was uniformly true in all tumor regions. To this end, we first quantified $CD3^+$ T cells
204 by immunofluorescent (IF) staining of 8µm sections. We classified each field of view as
205 predominantly occupied by CIT6-YFP cells ("YFP regions"; >60% of tumor cells are YFP^+),
206 predominantly occupied by CIT9-RFP cells ("RFP regions"; >60% of tumor cells are RFP^+), or
207 mixed ("mixed regions"; YFP and RFP each represent more than 40% of tumor cells), and then
208 quantified the number of $CD3^+$ T cells in the field (**Fig. 3A**). This analysis revealed a significantly
209 higher average count of $CD3^+$ T cells in YFP regions compared to RFP regions, with mixed
210 regions showing an intermediate level (**Fig. 3B**). Further, we observed a significant positive
211 correlation between the number of T cells and the fraction of YFP tumor cells (R^2=0.22, p=4.7 x
212 10^{-35}) in each field, and noticed that the fields of view with the highest number of infiltrating T
213 cells were all comprised of >50% YFP^+ cells (**Fig. 3C**). These data suggest that T cells
214 preferentially localize to the regions occupied by CIT6-YFP tumor cells in mixed-population
215 tumors.
216 We next turned to flow cytometry-based analysis of the immune cells in each YFP,
217 mixed, and RFP regions to gain a higher dimensional profile of the immune response in each
218 region. Mixed population tumors were embedded into agarose gel and each tumor was sliced

219 into five to ten 400µm-thick live sections. Each section was manually microdissected into YFP,
220 mixed, and RFP regions using a surgical scalpel under a fluorescent dissecting microscope. All
221 YFP pieces, all mixed pieces, and all RFP pieces from the same tumor were pooled and digested
222 into a single cell suspension for immune profiling by flow cytometry (**Fig. 3D**). Mirroring our
223 findings by IF, we found a higher frequency of total $CD3^+$ T cells in YFP regions than in RFP
224 regions, with mixed regions showing intermediate infiltration **(Fig. 3E)**. This localization pattern
225 was also seen in, and was driven by, CD4 T cells. The abundance of total T cells and CD4 T cells
226 in YFP regions of mixed-population tumors was comparable to that in single-population CIT6-
227 YFP tumors, and similarly, the abundance of total and CD4 T cells in RFP regions of mixed
228 tumors was comparable to that in single-population CIT9-RFP tumors (**Fig. 3F**). By contrast, CD8
229 T cells were at low abundance in all tumor regions, including YFP regions, and were found at
230 levels resembling those in single-population CIT9-RFP tumors (**Fig. 3G**). A more detailed analysis
231 of T cell function showed that nearly one-third of the CD4 T cells in YFP regions were Th1 cells
232 ($CD4^+$ $IFN\gamma^+$), whereas only ~2% of CD4 T cells in RFP regions were Th1 cells (median frequency
233 of Th1 cells in YFP regions = 28.9%, RFP regions = 1.99%) (**Fig. 3H**). Th2 ($CD4^+$ $IL\text{-}4^+$) and Th17
234 ($CD4^+$ $IL\text{-}17^+$) cells were equally rare in all regions (**Fig. 3I**). Even more strikingly, despite their
235 low abundance, CD8 T cells showed increased effector function in YFP regions: over 70% of CD8
236 T cells in YFP regions showed capacity to produce IFNγ, whereas less than 10% of CD8 T cells in
237 mixed and RFP regions showed the same (**Fig. 3J**). There was no apparent difference in Treg
238 ($Foxp3^+$ $CD25^+$) cell frequency between regions, but the ratio of Treg:Th1 cells and Treg: $IFN\gamma^+$
239 CD8 T cells was higher in RFP regions compared to YFP and mixed regions, suggestive of an
240 overall more immunosuppressive microenvironment in RFP regions (**Fig. 3J, K**). In addition,

241 macrophages (F4/80^{+} CD11b^{+} MHC-II^{+}) were significantly enriched in mixed regions compared
242 to YFP regions, and also trended toward higher enrichment in RFP regions (**Fig. 3L**).
243 Collectively, these data show that local tumor cells themselves play a significant role in
244 driving the immune microenvironment in their vicinity. Moreover, the observation that mixed
245 regions look similar to RFP regions—in terms of effector T cell infiltration and macrophage
246 infiltration—suggests that in regions in which both CIT6-YFP and CIT9-RFP tumor cells co-exist,
247 cold CIT9-RFP tumor cells exert dominance over the local immune infiltrate. The "dominant
248 coldness" of CIT9-RFP is also seen in the global suppression of CD8 T cell infiltration in all
249 regions. However, CD8 T cells that managed to infiltrate YFP regions show a highly active
250 phenotype.
251
252 **CD206^{Hi} macrophages and lack of neutrophils and monocytes mediate an immunosuppressive**
253 **TME in RFP regions.**

254 To characterize immune cell spatial patterning more deeply, we employed ZipSeq spatial
255 transcriptomics[25] to CIT6-YFP + CIT9-RFP mixed-population tumors. ZipSeq allows immune cells
256 within user-defined regions of interest in live tissue sections to be tagged with distinct
257 nucleotide sequences (akin to assigning each region of interest a unique zip code), making use
258 of photocaged oligonucleotides and precise light exposure. Using this method, immune cells
259 from YFP, RFP and mixed regions of mixed population tumors (n=2) were tagged with distinct
260 "zip code" barcodes, and sections were subsequently disaggregated and subjected to single cell
261 RNA sequencing (scRNA-seq) (**Fig. 4A**). Immune cells were subjected to UMAP clustering, and
262 cluster identities were assigned based on expression of well-established markers (**Fig. 4B**, Supp

263 Fig. 5A, B). Using ZipSeq barcodes, we mapped each immune cell back to the region it
264 originated from. In line with our flow cytometry analyses, we observed a higher infiltration of T
265 cells in YFP regions compared to RFP regions (**Fig. 4C, D**), and also saw that myeloid cells
266 comprised a majority of the immune cells (**Fig. 4B**). In particular, we observed three large
267 macrophage clusters, CD206^{Hi} macrophages, MHC-II^{Hi} macrophages, and Arg1^{Hi} macrophages
268 (**Fig. 4B,** Supp Table 1). These three clusters were all enriched in RFP regions (**Fig. 4E**). By
269 contrast, neutrophils and monocytes were observed at lower abundance in RFP regions than
270 YFP regions (**Fig. 4F, G**). We carried out ZipSeq single cell spatial transcriptomics on a second
271 mixed-population tumor, and found similar results (Supp Fig. 6). Myeloid cells comprised a
272 majority of the immune cells (Supp Fig. 6A-C) and T cells were enriched in YFP regions (Supp Fig.
273 6D, E). Notably, out of seven macrophage clusters in the second tumor, six of them were
274 enriched in RFP regions compared to YFP regions (Supp Fig. 6F). Moreover, the second tumor
275 showed enrichment of neutrophils and monocytes in YFP regions (Supp Fig. 6G, H). Pathway
276 analysis with EnrichR, using genes enriched in each cluster and the GO Biological Process 2021
277 repository, suggested neutrophils had pro-inflammatory properties, as seen by neutrophil
278 activation-related genes (**Fig. 4F**, Supp Fig. 6G). Monocytes also exhibited evidence of
279 activation, with a particularly clear pro-inflammatory signature in the second tumor (**Fig. 4G**,
280 Supp Fig. 6H). Together, the combination of an enrichment of immunosuppressive
281 macrophages and a de-enrichment of inflammatory monocytes and neutrophils point to a
282 myeloid cell-driven immunosuppressive TME in RFP regions.
283
284 **Chemokine CX3CL1 is a mediator of the CIT9-RFP-driven immunosuppressive TME.**

285 To identify the drivers behind the striking spatial organization of myeloid cell infiltrates
286 in our mixed tumors, we next assessed the protein expression of a total of 44 cytokines and
287 chemokines using the lysates from CIT6-YFP and CIT9-RFP tumors. Cytokines and chemokines
288 are major mediators of immune cell localization and function, thus we hypothesized differences
289 in their expression between CIT6-YFP and CIT9-RFP might explain the differences we saw in
290 myeloid infiltrate. We found the chemokine CX3CL1 was significantly enriched in CIT9-RFP
291 tumors compared to CIT6-YFP tumors (**Fig. 5A**, Supp Fig. 7A). CX3CL1 is a chemokine with
292 reported pro-tumor properties, capable of directly promoting tumor cell proliferation and
293 migration as well as of attracting various immune cell types[26,27]. To test the hypothesis that
294 CX3CL1 plays a role in driving the immunosuppressive microenvironment in our squamous cell
295 carcinomas, we generated a CIT6-YFP cell line overexpressing *Cx3cl1* and analyzed the immune
296 profile of these tumors. The abundance of macrophages was increased in Cx3cl1-
297 overexpressing tumors compared to control tumors (**Fig. 5B**). We next asked if it was a
298 particular macrophage subset(s) that showed increased abundance, and for this analysis
299 divided macrophages into the 3 main clusters we identified in our ZipSeq analysis: CD206^{Hi}
300 macrophages (CD206^{Hi} MHC-II^{Low}), MHC-II^{Hi} macrophages (CD206^{Mid} MHC-II^{Hi} Arg1^{-}) and Arg1^{Hi}
301 macrophages (CD206^{Mid} MHC-II^{Hi} Arg1^{+}) (Supp Fig. 7B). We found that CD206^{Hi} macrophages
302 were increased in frequency in CX3CL1-overexpressing CIT6-YFP tumors compared to control
303 tumors, while the other two macrophage subsets showed no difference in frequency (**Fig. 5C**).
304 In line with this, expression of CX3CR1, a cognate receptor of CX3CL1, was the highest on
305 macrophages among all immune cell types (Supp Fig. 7C), and highest on CD206^{Hi} macrophages
306 among the three macrophage subsets (**Fig. 5D**). Additionally, we observed a lower abundance

307 of neutrophils (Ly6G^{+}) and monocytes (Ly6C^{+}) in CX3CL1-overexpressing CIT6-YFP tumors (**Fig.**
308 **5E**). Other immune cell types including B cells, CD8 T cells and DCs showed no difference in
309 frequency (Supp Fig. 7D).

310 We next asked whether CD206^{Hi} macrophages, as the main macrophage subtype
311 increased by CX3CL1 overexpression, had a greater capacity to suppress T cells than non-
312 CD206^{Hi} macrophages (which include both MHC-II^{Hi} and Arg1^{Hi} macrophages). We isolated
313 CD206^{Hi} and non-CD206^{Hi} macrophages from CIT9-RFP and CIT6-YFP tumors by flow cytometry-
314 based sorting (Supp Fig. 7B) and tested for their ability to suppress CD8 T cell proliferation using
315 an *in vitro* co-culture assay. We found that CD206^{Hi} macrophages could suppress T cell
316 proliferation and activation even at a low macrophage-to-CD8 T cell ratio (1:16), whereas non-
317 CD206^{Hi} macrophages could suppress CD8 T cells only at a higher co-culture ratio (1:4) (**Fig. 5F**,
318 Supp Fig. 7E). Thus, while both CD206^{Hi} and non-CD206^{Hi} macrophages exhibited suppressive
319 capacity to some extent, the CD206^{Hi} macrophage subset in our tumors has a particularly strong
320 ability to suppress T cell proliferation.

321 Because we also observed an enrichment of CD206^{Hi} macrophages and lower
322 abundance of neutrophils and monocytes in RFP regions of mixed-population tumors in our
323 ZipSeq data (**Fig. 4**), we hypothesized that the CX3CL1-CX3CR1 axis plays a role in driving the
324 immunosuppressive microenvironment in these regions. There were few reads of *Cx3cl1* in the
325 ZipSeq data (data not shown) likely due to limitations associated with single cell RNAseq.
326 Therefore, to test this hypothesis, we assessed the correlation between the *Cx3cr1* expression
327 level in immune cells and their abundance in RFP regions. *Cx3cr1* transcript level was high in
328 clusters that were enriched in RFP regions (**Fig. 5G** and **Fig. 4C**; Supp Fig. 8A and Supp Fig. 6D),

329 and was the highest on the CD206^{Hi} macrophage cluster (**Fig. 5H**, Supp Fig. 8B). Moreover,
330 there was a positive correlation across clusters between the abundance of a cluster and its
331 average *Cx3cr1* transcript expression level in RFP regions, but not in YFP or mixed regions (**Fig.**
332 **5I**). Collectively, these data indicate that CX3CL1 plays a role in driving local myeloid cell
333 abundance and enriching immunosuppressive CD206^{Hi} macrophages in RFP regions of mixed-
334 population tumors.
335
336 **CX3CL1 is a mediator of a cold TME in human cancers.**
337 To assess the role of CX3CL1 in shaping the TME and myeloid cell abundance in human cancers,
338 we turned to a previously published pan-cancer human dataset containing transcriptomic
339 profiles of whole tumors and of individual immune compartments (e.g., myeloid compartment)
340 from 364 individual tumors across 12 cancer types[28]. Previous analysis identified 12 recurrent
341 immune infiltration patterns across these 364 tumors, denoted "immune archetypes", spanning
342 a range from immune rich to immune poor TMEs. Looking at T cell abundance, 7 of these
343 archetypes could be classified as immune hot and 5 of them as immune cold, corresponding
344 with high and low T cell infiltrates based on T cell transcriptomic scores **(Fig. 6A).** We assessed
345 whole-tumor *CX3CL1* RNA expression in each archetype, and found that, strikingly, *CX3CL1*
346 levels were highest in 3 of 5 cold archetypes (archetypes 9, 10 and 12) and comparatively low in
347 all hot archetypes **(Fig. 6B)**. Next, we examined the macrophage:monocyte ratio across all
348 human archetypes, using transcriptomic scores for macrophages and monocytes based on
349 RNAseq data from the myeloid compartment of each tumor.[28] We observed a bias in the
350 myeloid compartment toward macrophages (log2 of the macrophage:monocyte ratio > 0) in the

351 same 3 cold human archetypes that showed high *CX3CL1* (archetypes 9, 10, and 12, **Fig. 6C**).
352 Using a gene signature based on the CD206^{hi} cluster in our ZipSeq dataset, we also asked if
353 CD206^{hi} macrophages were enriched in *CX3CL1*-high human immune archetypes. We found
354 that, among cold archetypes, the macrophage compartment showed a high CD206^{hi}
355 macrophage score in 2 archetypes, both of which were *CX3CL1*-high (archetypes 10 and 12, **Fig.**
356 **6D**). Finally, we turned back to our CX3CL1-overexpressing mouse tumors. We saw that CX3CL1
357 overexpression led to an increase in both the macrophage:monocyte ratio and the CD206^{hi}
358 macrophage: non-CD206^{hi} macrophage ratio in CX3CL1-overexpressing CIT6-YFP tumors
359 compared to controls **(Fig. 6E)**. Of note, we also analyzed the 7 hot human archetypes that
360 show low *CX3CL1* expression, and found a range of macrophage:monocyte ratios and CD206^{hi}
361 macrophage scores (Supp. Fig.9), suggesting that additional and likely different factors shape
362 these ratios in hot, CX3CL1-low tumors. Collectively, these data show that CX3CL1 is associated
363 with cold TMEs enriched in CD206^{hi} macrophages not only in our mouse model, but also across
364 multiple human cancers.
365

366 **An immunosuppressive tumor population drives resistance of mixed-population tumors to**
367 **anti-PD-1 blocking and CD40 agonistic antibody combination treatment.**

368 Having shown that CIT9-RFP tumor cells in mixed-population heterogeneous tumors
369 exert a dominant immunosuppressive effect and drive spatial organization within the tumor,
370 we next sought to determine if the presence of CIT9-RFP tumor cells impacts the response of
371 mixed-population tumors to immune checkpoint blockade (ICB) therapy. In particular, as an
372 immunosuppressive tumor microenvironment is linked to resistance to ICB therapy, we asked if

373 CIT9-RFP tumor cells make otherwise therapy-sensitive CIT6-YFP tumor cells resistant. We
374 tested multiple ICB combinations on our tumors, and we selected a regimen combining PD-1
375 blockade and CD40 agonist antibodies, a combination that is currently in clinical trials for
376 multiple tumor types. The combination treatment was administered in two doses at a 3-day
377 interval when the CIT6 and CIT9 tumors reached 5mm in diameter (**Fig. 7A**) and induced 50% of
378 CIT6-YFP tumors (5 out of 10 tumors) to regress completely, with 2 tumors eventually growing
379 back after 5-17 days (**Fig. 7B**). In contrast, only 9% (1 out of 11) of CIT9-RFP tumors showed a
380 decrease in tumor volume after therapy, and none achieved a complete regression (**Fig. 7B**).
381 Furthermore, the increase in the average volume of CIT6-YFP tumors over time was blunted by
382 the combination treatment in comparison to isotype control treatment, whereas CIT9-RFP
383 tumors showed similar growth kinetics in both combination treatment and isotype control arms
384 (**Fig. 7B**). This coincided with prolonged overall survival of the mice harboring CIT6-YFP tumors,
385 but not CIT9-RFP tumors, after treatment with the combination therapy (**Fig. 7C**). Thus, the
386 combination of anti-PD-1 blocking and CD40 agonistic antibodies mimics prototypical patient
387 outcomes to immunotherapy where immune hot tumors respond and immune cold tumors do
388 not. Further, this combination showed the clearest dichotomy in responses between hot and
389 cold tumors among the regimens tested, and so we chose to proceed with using it to
390 investigate how mixed-population tumors would respond.
391 We then assessed the response of tumors derived from a 1:1 mixture of CIT6-YFP and
392 CIT9-RFP cell lines to the anti-PD-1 blocking and CD40 agonist combination treatment. The
393 combination therapy achieved complete regression (CR) in 1 out of 23 mice (4.3%) but the
394 tumor quickly grew back (**Fig. 7D**). The CR rate of mixture-derived tumors was higher than CIT9-

395 RFP single-population tumors (0% CR), but lower than CIT6-YFP tumors (50% CR) (**Fig. 7B, D**).
396 The average tumor volume was slightly smaller in the combination treatment group (**Fig. 7D**),
397 although this did not correlate to an extension of overall survival (**Fig. 7D**), suggesting therapy
398 had only a modest effect in these mixed tumors.

399 Immune profile analysis of tumors at the time of harvest (10mm in diameter) revealed
400 that CD4 and CD8 T cell infiltration was increased in both CIT6-YFP tumors and mixed tumors
401 treated with the anti-PD-1 + anti-CD40 agonist combination, and that this influx was of similar
402 magnitude in both (**Fig. 7E**). By contrast, CIT9-RFP tumors did not show a change in T cell
403 infiltration after treatment (**Fig. 7E**). However, despite the influx of T cells into mixed tumors,
404 this influx did not correspond to the same level of treatment efficacy seen in CIT6-YFP tumors.
405 Collectively, these data suggest that the presence of CIT9-RFP tumor cells dampens the
406 response of mixed tumors to the combination treatment, and also reveals an improved influx of
407 T cells into the tumor after treatment is not necessarily a marker of a successful response in the
408 context of a heterogeneous tumor.

409

410 **Spatial immune infiltration patterns persist in mixed-population tumors following anti-PD-1**
411 **blockade and CD40 agonist combination treatment.**

412 Given our previous data showing that RFP regions (and to a lesser extent, mixed regions)
413 of mixed-population tumors were spatially organized pockets of immune coldness, we sought
414 to test the hypothesis that the immunotherapy combination treatment was acting successfully
415 in YFP regions, but failing to improve the immune response in RFP regions, leading to overall
416 failure. We applied our live tumor slice microdissection technique (**Fig. 3D**) to mixed-population

417 tumors treated with either anti-PD-1 blockade + CD40 agonist or control antibodies. The
418 immune infiltration profiles of YFP, RFP and mixed regions were analyzed 6 days after the initial
419 treatment dose, at which point tumors have not started to shrink yet (**Fig. 7B and D**). We
420 focused our analysis on T cells, as we had observed that T cell infiltration was increased by the
421 combination treatment in mixed population tumors (**Fig. 7E**).

422 At the 6-day timepoint, the frequencies of overall CD4 and CD8 T cells did not differ
423 between the isotype control arm and the combination treatment arm in any of the three
424 regions (Supp Fig. 10). However, the presence of Th1 cells was dramatically increased in RFP
425 and mixed regions by the combination treatment compared to isotype control treatment (**Fig.**
426 **8A**). There was also a trend toward increased Th1 cells in YFP regions, but it did not reach
427 statistical significance. The treatment-induced change in abundance was unique to Th1 cells, as
428 other CD4 T cell subsets including Treg, Th2 and Th17 cells showed a similar frequency between
429 isotype control and combination treatment arms (**Fig. 8B, C**). The changes in Th1 cell
430 abundance resulted in a favorable increase in the Th1:Treg ratio in mixed and RFP regions of
431 the combination therapy-treated tumors (**Fig. 8D**). The functional impact on the CD8 T cell
432 compartment was directionally the same, but much less dramatic. The frequency of IFNγ^+ CD8 T
433 cells was modestly increased by the combination therapy in RFP regions, but not in mixed
434 regions (**Fig. 8E)**, and the IFNγ^+ CD8 T cell to Treg ratio showed a trend of improvement in mixed
435 and RFP regions in response to the treatment (**Fig. 8F**). However, because the abundance of
436 CD8 T cells remained low in all regions (as previously observed in mixed-populations tumors,
437 Fig. 3G), these improvements in CD8 T function were of small magnitude on an absolute scale.
438 Collectively, these data show that anti-PD-1 and CD40 agonist antibody treatment was

439 successful at improving the quality of the immune response in cold RFP and mixed tumor
440 regions—contrary to our expectations that we would only observe such improvements in the
441 hot YFP regions. However, despite the therapy-induced boost, the quality of the immune
442 response in RFP regions remained inferior to that in YFP regions, and the absolute number of
443 tumor-infiltrating CD8 T cells remained low. Thus, while the therapy-induced improvement in
444 anti-tumor Th1 CD4 T cell response in RFP and mixed regions likely contributed to the blunted
445 growth of treated tumors—which was also seen in this 6-day cohort (**Fig. 8G**)—it was largely
446 insufficient to mediate tumor rejection.
447
448 **Discussion**
449 Combining fluorescently tagged pro-inflammatory (hot) and immunosuppressive (cold)
450 squamous cell skin carcinoma tumor populations, we have developed a novel model system to
451 interrogate the spatial heterogeneity of tumor cells and intratumoral immune cells. When
452 combined in a 1:1 ratio, we see that an immunosuppressive tumor population has a "dominant
453 negative" suppressive effect, in line with a previous report in a model of pancreatic cancer[15].
454 The overall immune phenotype of mixed-population tumors most closely resembles that of
455 cold, immunosuppressive tumors, and exhibits a poor infiltration of CD8 T cells—which are
456 critical to anti-tumor immunity—in all regions. Moreover, the dominant effect of the
457 immunosuppressive tumor population is also seen locally in "mixed" regions where the two
458 tumor populations co-exist.
459 However, when we look at regions locally dominated by hot tumor cells (YFP^+ regions in
460 our tumors), we find CD4 T cells accumulate specifically in these regions, as do inflammatory

461 monocytes and neutrophils. Both CD4 and CD8 T cells also show better effector phenotypes in
462 the vicinity of hot tumor cells. By contrast, immunosuppressive macrophages preferentially
463 accumulated in the neighborhoods of cold tumor cells. Tumor cells themselves thus set up a
464 blueprint for the spatial architecture of infiltrating immune cells, with different tumor cell
465 populations driving distinct "micro-microenvironments" in their vicinities. Our study is the first,
466 to our knowledge, to demonstrate a clear, reproducible link between spatial organization of
467 infiltrating immune cells and the underlying spatial organization of tumor cells.

468 Tumor cell-driven spatial differences in the intratumoral immune response exist at
469 baseline in the absence of therapy, but also persist during immunotherapy and exert an
470 influence on the response to therapy. Regional analysis of response to anti-PD-1 blockade +
471 anti-CD40 agonist combination immunotherapy showed a more nuanced pattern than we
472 expected: Rather than seeing a simplistic "good" response in hot regions and "poor" response
473 in cold regions, the relative influx of Th1 cells and IFNγ^+ CD8 T cells was strongest in RFP$^+$ cold
474 regions. Nonetheless, cold regions remained more poorly infiltrated than hot regions at an
475 absolute level, even after the therapy-induced boost, indicating that therapy did not entirely
476 overcome the spatial patterning that existed pre-treatment. While the anti-PD-1 plus CD40
477 agonist combination we employed failed to cure our mixed tumors, our model system
478 facilitated detailed region-by-region analysis of the effects and efficacy of therapy. This system
479 thus establishes a platform on which additional drug combinations or dose regimens can be
480 probed to iterate on how best to induce a productive tumor-wide anti-tumor immune response
481 across all tumor regions.

482 We identify CX3CL1 as a mediator of a myeloid-cell-centric immunosuppressive
483 microenvironment, and a candidate driver of the "pockets of coldness" we observe in our
484 heterogeneous tumors. We show that CX3CL1-expressing tumor cells drive enrichment of
485 immunosuppressive CD206^{Hi} macrophages, and depletion of inflammatory monocytes and
486 neutrophils. In a pan-cancer analysis of human patients, high levels of CX3CL1 are associated
487 with three specific immune cold TME archetypes, all of which show macrophage-enriched
488 myeloid compartments and 2 of the 3 show a specific enrichment of CD206^{Hi} macrophages. The
489 CX3CR1:CX3CL1 axis has also been found to be linked to macrophage accumulation in both skin
490 SCC and breast tumors on a whole-tumor level[29,30]. Further, our findings that CX3CL1 is a
491 candidate mediator of local immunosuppressive myeloid cell organization are in line with
492 previous reports of chemokine-driven spatial organization of immune cells within tumors[31,32].
493 Of note, CX3CL1 has also been described as an "anti-tumor" chemokine, particularly in lung
494 cancer, due to its role interacting with CX3CR1+ T cells,[26,33–35] highlighting that its role in tumor
495 immunity is context-dependent and not yet fully understood. Therefore, careful investigation
496 into CX3CL1 is essential to assess its potential therapeutic application. Of course, CX3CL1 does
497 not fully define the immune microenvironment. Future work, in addition to more deeply
498 investigating the role of CX3CL1, is also expected to uncover additional pathways by which
499 tumor cells shape their local micro-microenvironments and influence responses to
500 immunotherapy on a highly local spatial scale.
501
502 **Figure legends:**

503 **Figure 1. Modeling intratumoral heterogeneity using fluorescently-labeled DMBA/TPA-**

504 **induced squamous cell skin carcinoma cell lines.**

505 **(A-C)** Flow cytometric analysis of T cell infiltration in subcutaneous tumors derived from

506 injection of CIT6-YFP and CIT9-RFP cell lines into mice carrying an unactivated *Confetti* cassette.

507 **(D)** Immunofluorescent staining of $CD3^+$ T cells in 8µm cryosections of subcutaneous CIT6-YFP

508 and CIT9-RFP tumors, with DAPI staining cell nuclei, and quantification of T cell count per field

509 Scale bar = 100µm. **(E)** Schematic of mixed-population tumor generation. A 1:1 mixture of CIT6-

510 YFP and CIT9-RFP cell lines subcutaneously was injected into the right hind flank of mice

511 carrying an unactivated *Confetti* cassette, and the resulting tumors were harvested for

512 downstream analyses when they reached 1cm in diameter at 21-28 days post injection. **(F, G)**

513 Whole-tumor images by fluorescent dissecting microscope (F) and a representative image of a

514 tumor cross-section (8µm cryosection) (G) of tumors that were a 1:1 mixture of CIT6-YFP and

515 CIT9-RFP cell lines. Scale bars in (F) and (G) are 2mm and 1mm respectively. All data are a

516 representation of at least 3 independent experiments.

517

518 **Figure 2. The immunosuppressive tumor population drives an overall immunosuppressive**

519 **phenotype in mixed-population tumors.**

520 **(A-E)** Flow cytometric immune profiling of tumors derived from CIT6-YFP and CIT9-RFP cell lines

521 and mixed-population tumors derived from a 1:1 mixture of the two cell lines, including **(A)** T

522 cells, CD4 T cells and CD8 T cells, **(B)** frequency of tumor cells ($CD45^-$ YFP^- or $CD45^-$ RFP^-)

523 expressing MHC-I molecules (H2-K^q and H2-L^qD^q) (left) and median fluorescence intensity (MFI)

524 of the MHC-I molecules on H2-K^q and H2-L^qD^q double positive tumor cells (right), **(C)** Treg

525 (Foxp3$^+$ CD25$^+$) frequency, CD8 T cell-to-Treg ratio, and effector CD4 T cell (Teff, Foxp3$^-$ CD25$^-$)-
526 to-Treg ratio, **(D)** B cells (B220$^+$) and natural killer (NK) or innate lymphoid cell (ILC) (NKp46$^+$)
527 lymphocytes and **(E)** macrophages (F4/80$^+$ CD11b$^+$ MHC-II$^+$). Data in (A)-(E) are a representation
528 of at least two independent experiments with ≥5 mice per experiment. **(F-H)** *In vitro* CD8 T cell
529 suppression by macrophages sorted from the tumors. CFSE-stained and CD3/28 beads-
530 stimulated CD8 T cells isolated from naïve *Confetti* mice were co-cultured with tumor-
531 associated macrophages (TAM) at varying ratios (50K T cells and 12.5K, 25K, or 50K TAMs) and
532 analyzed for proliferation via CFSE signal and activation markers. Data are a representation of 2
533 independent experiments, with 3 biological replicates in each experiment. **(F)** Representative
534 histogram showing the CFSE signal in CD8 T cells, with gates marking divided cells, defined as
535 the cells that have divided more than twice in no TAM condition or 50K T cell + 50K TAM
536 conditions (left) and graph showing the count of divided cells (right). "No TAM", T cell
537 stimulation control without macrophages; "No stim", control with no T cell stimulation. **(G)**
538 Count of activated (CD69$^+$ CD25$^+$) CD8 T cells, **(H)** Count of effector CD8 T cell subsets marked
539 by combinations of CD62L and CD44 expression.
540
541 **Figure 3. Spatial organization of tumor populations drives the spatial organization of immune**
542 **cells.**
543 **(A)** Representative cross-section images showing examples of a YFP, mixed and RFP region of a
544 mixed-population tumor and CD3 stain. **(B)** Quantification of CD3$^+$ T cells per field, plotted for
545 each region. **(C)** Correlation of YFP$^+$ cell fraction and CD3$^+$ T cell frequency in each field. CD3$^+$ T
546 cell count was scaled to DAPI$^+$ cell count in each field to normalize the difference in cell density

547 between fields. **(D)** Schematic of immune cell profiling in YFP, mixed and RFP regions of mixed-
548 population tumors. Each mixed-population tumor was sliced into five to ten 400µm-thick live
549 sections, and each section was manually microdissected into YFP, mixed, and RFP regions using
550 a surgical scalpel under a fluorescent dissecting microscope. All YFP pieces, all mixed pieces,
551 and all RFP pieces from the same tumor were pooled for immune profiling by flow cytometry.
552 White scale bar = 5mm, blue scale bar = 1mm. **(E-L)** Frequency of T cell subsets, ratio of Treg to
553 IFNγ^+ CD8 T cells or Th1 cells, and frequency of macrophages in YFP, mixed and RFP regions.
554 Grey dotted lines in panels (E), (F), (G) and (L) separate data of mixed-population tumors from
555 the data of single-population tumors. All data are a representation of two independent
556 experiments, with ≥3 mice per experiment (B,C) or ≥6 mice per experiment (E-L).
557
558 **Figure 4. CD206^{Hi} macrophages and lack of neutrophils and monocytes mediate an**
559 **immunosuppressive TME in RFP regions.**
560 **(A)** Schematic of ZipSeq spatial transcriptomic analysis of mixed-population tumors. Composite
561 stitched image of a 200µm-thick live section marked with YFP regions (encircled with green
562 lines), RFP regions (red lines) and mixed regions (blue lines) is shown. YFP, RFP and mixed
563 regions were illuminated individually to allow for the binding of a unique barcode ("zipcode") to
564 a photocaged oligo-CD45 antibody complex. ZipCode-tagged immune cells were analyzed by
565 scRNAseq. **(B)** Uniform manifold approximation and projection (UMAP) representation of
566 zipcode-labeled cells with cluster overlay. n = 3,238 cells, n_{YFP} = 1,236, n_{RFP} = 1,318, n_{Mixed} = 684.
567 **(C)** UMAP representation of zipcode-labeled cells with zipcode identity overlaid. **(D)** Abundance
568 of cells belonging to the T cell cluster (cluster 9), calculated as percentage of total immune cells

569 in each region. **(E)** Abundance of cells belonging to MHC-II^{Hi}, Arg1^{Hi} and CD206^{Hi} macrophage
570 clusters (clusters 1, 2, and 3 respectively), calculated as percentage of total immune cells in
571 each region. **(F)** Percentage of cells belonging to neutrophil cluster (cluster 7) in each region and
572 pathway analysis showing the gene families enriched in the neutrophil cluster based on the top
573 250 differentially expressed genes. **(G)** Percentage of cells belonging to monocyte cluster
574 (cluster 6) and pathway analysis of genes enriched in the monocyte cluster based on the top 31
575 differentially expressed genes.
576
577 **Figure 5. Chemokine Cx3cl1 mediates the CIT9-RFP-driven immunosuppressive TME.**
578 **(A)** ELISA-based quantification of CX3CL1 using tumor lysates of CIT6-YFP and CIT9-RFP single-
579 population tumors (n=3 per cell line) **(B, C)** Infiltration of total macrophage (B) and macrophage
580 subsets (C) in CIT6-YFP tumors overexpressing CX3CL1 (CIT6-YFP^{Cx3cl1}) and empty vector (CIT6-
581 YFP^{Empty}). **(D)** Expression of CX3CR1 on macrophage subsets in CIT6-YFP^{Cx3cl1} tumors, measured
582 as MFI from flow cytometric analysis. **(E)** Frequency of neutrophils and monocytes in CX3CL1-
583 overexpressing CIT6-YFP tumors. Data in (B)-(E) are representation or combination of two
584 independent experiments with ≥10 mice per experiment. **(F)** CD8 T cell suppression assay using
585 CD206^{Hi} macrophages and a pool of Arg1^{Hi} macrophages and MHC-II^{Hi} macrophages (Non-
586 CD206^{Hi} TAMs) isolated from CIT6-YFP and CIT9-RFP single-population tumors. Representation
587 of two independent experiments with at least 2 mice per arm. **(G)** Feature plot overlaid on
588 UMAP representation for *Cx3cr1* gene from the tumor analyzed by ZipSeq in Fig. 4. **(H)** Violin
589 plot showing *Cx3cr1* distribution based on cluster identity. **(I)** Correlation between an average

590 relative *Cx3cr1* transcript level of each cluster and the percentage of cells belonging to the
591 cluster. Combined analysis of two tumors analyzed in Fig. 4 and Supp Fig. 6.
592
593 **Figure 6. CX3CL1 is a mediator of a cold TME in human cancers.**
594 **(A-D)** Analysis of immune cells and *CX3CL1* expression using a previously published dataset of
595 364 human tumors from 12 cancer types. Computational clustering of tumors using flow
596 cytometry data and transcriptomic data enabled identification of 12 dominant patterns of
597 immune composition across various cancers, referred to as immune archetypes (ref. 28).
598 RNAseq data was generated separately for all viable cells and for sorted mononuclear
599 phagocytes. Prior to RNA sequencing, cells were sorted by flow cytometry from untreated,
600 freshly resected human tumors. **(A)** T cell score of each tumor, based on RNAseq of all viable
601 cells, grouped on the x-axis by immune archetype. **(B)** Heatmap of average *CX3CL1* RNA
602 expression, based on RNAseq of all viable cells, for each immune archetype. **(C)** Ratio of
603 macrophage score and monocyte score, based on RNAseq of mononuclear phagocytes, for
604 tumors in the 5 cold immune archetypes. **(D)** $CD206^{Hi}$ macrophage score, based on RNAseq of
605 mononuclear phagocytes, for tumors in the 5 immune cold archetypes. **(E)** Ratio of
606 macrophages to monocytes (left) and $CD206^{Hi}$ macrophages to non-$CD206^{Hi}$ macrophages
607 (right) detected in mouse CIT6-YFP tumors overexpressing *Cx3cl1* or controls.
608
609 **Figure 7. An immunosuppressive tumor population drives resistance of mixed-population**
610 **tumors to anti-PD-1 blocking and CD40 agonistic antibody combination treatment.**

611 **(A)** Dosing schedule of anti-PD-1 and CD40 agonist treatment. **(B)** Tumor growth curves of CIT6-
612 YFP and CIT9-RFP tumors showing tumor volume of individual tumors and average volume of
613 isotype control and anti-PD-1+CD40 agonist combination treatment arms. Red arrows under
614 the x axis shows the timing of treatments (day 0 and 3), fraction shown on the top right corner
615 of individual tumor volume plots shows the number of mice whose tumors completely
616 regressed post-treatment. **(C)** Kaplan-Meier curves comparing the survival of mice from each
617 treatment arm. Statistical test was performed using log-rank test. **(D)** Tumor growth and
618 survival of mice harboring tumors derived from a 1:1 mixture of CIT6-YFP and CIT9-RFP cell
619 lines. **(E)** Frequency of tumor-infiltrating T cells post-treatment in CIT6-YFP, CIT9-RFP, and 1:1
620 mixture-derived tumors. All experiments were performed with at least 8 mice per treatment
621 arm.
622
623 **Figure 8. Spatial immune infiltration patterns persist in mixed-population tumors following**
624 **anti-PD-1 blockade and CD40 agonist combination treatment.**
625 **(A–F)** Tumors derived from a 1:1 mixture of CIT6-YFP and CIT9-RFP cell lines were treated with
626 α-PD-1 +CD40 agonist combination treatment or isotype control antibodies at day 0 and 3 and
627 analyzed at day 6 for spatial T cell infiltration profile via microdissection and flow-based
628 analysis. **(A)** Th1 cell frequency in each region of isotype control-treated and combination
629 therapy-treated tumors, **(B)** Treg frequency, **(C)** Frequency of Th1, Th2, Th17 and Treg cells, **(D)**
630 Th1-to-Treg ratio, **(E)** Frequency of IFNγ^+ CD8 T cells and **(F)** IFNγ^+ CD8 T cell to Treg ratio. **(G)**
631 Average tumor volume of each treatment arm. Red arrows under the x axis shows the timing of
632 treatments. Experiment was performed with at least 10 mice per treatment/tumor arm.

633

634

635

636 **Materials and methods:**

637 Carcinogenesis and cell line generation

638 To induce tumors, *K5-CreER^{T2}-Confetti FVB/N* mice were treated with 25 mg DMBA followed by

639 TPA (200 µl of a 10^{-4} M solution in acetone) two times a week for 20 weeks, as described[19]. To

640 generate cell lines, carcinomas were resected at a size of >1 cm in longest diameter, finely

641 chopped, digested in DMEM containing Collagenase I and IV and DNase I for 45 minutes at

642 37 °C, washed with PBS, plated in supplemented DMEM (high-glucose DMEM (Gibco, catalog#

643 11995065) plus 10% heat-inactivated FBS (Gibco), 2mM L-glutamine, with 100 units/ml

644 penicillin, 100 µg/ml streptomycin, and 2.5 µg/ml amphotericin B (Gibco)), and passaged until

645 cells stably grow in culture. The established cell lines were cultured in the supplemented DMEM

646 for all experiments.

647

648 Cell line labeling

649 Unlabeled cell lines were treated with adenoviral Cre recombinase (Vector Biolabs catalog

650 #1045) to induce labeling with Confetti fluorescent proteins. YFP- and RFP-expressing cells were

651 sorted via fluorescence-activated cell sorter and further grown in vitro to establish CIT6-YFP and

652 CIT9-RFP cell lines.

653

654 In vivo experiments

655 A total of 1.25 x 10^5 cells were injected subcutaneously into the dorsal flank of 8 to 16 week-old
656 male and female *Confetti*-homozygous *FVB/N* mice. Approximately 21-28 days later, when
657 tumors measured ~1cm in diameter, tumors were dissected and digested as described above,
658 and subsequently used in flow cytometric analysis. For treatment experiments, when tumors
659 measured approximately 5mm in diameter, mice were injected intraperitoneally with one dose
660 (CD40 agonistic antibody) or two doses (anti-PD-1 antibody) of therapeutic antibodies,
661 administered at a three day interval. Antibodies used were rat anti-mouse PD-1 IgG2a antibody
662 (RMP1-14, BioXCell), rat anti-CD40 agonist IgG2a antibody (FGK4.5, BioXCell), and rat IgG2a
663 isotype control (2A3; BioXCell) at 200µg per antibody per dose. Tumors were resected at 1cm in
664 diameter and used for downstream analyses, except in 6-day post-treatment analyses where
665 tumors were resected 6 days after treatment initiation. All animal experiments were approved
666 by the University of California San Francisco Laboratory Animal Resource Center (IUCAC;
667 AN187679). This work complies with all the relevant ethical regulations regarding animal
668 research.
669
670 <u>Flow cytometric immune profiling and macrophage cell sorting</u>
671 For whole tumor analysis and sorting, 5 million cells were stained with antibodies. For spatial
672 immune profiling, tumors were embedded in 2% agarose gel, sliced into 400µm section by a
673 Leica Vibratome, microdissected into YFP, RFP and mixed regions using surgical scalpel while
674 visualizing each region on MVX10 fluorescent stereoscope. Multiple pieces of each region from
675 a single tumor were pooled for digestion, followed by flow cytometric analysis. Cell sorting was

676 performed on FACS Aria III (BD Biosciences). Antibodies used for flow cytometric analyses and
677 sorting are listed in Table 2.
678
679 Immunofluorescence imaging
680 After half of the tumors were processed for flow cytometric analysis, the remaining halves were
681 fixed in 4% paraformaldehyde for 2 hours, dehydrated in PBS with 30% sucrose overnight at
682 4C°, embedded in Tissue-tek O.C.T. compound (Sakura Finetek USA) and stored at -80C°.
683 Embedded blocks were cryosectioned into 8µm sections using Leica CM3050 S Cryostat (Leica
684 Biosystems) and stained with rabbit anti-mouse CD3 antibody (ab5690, Abcam) overnight,
685 followed by stain with secondary anti-rabbit Alexa Fluor 647 antibody (Invitrogen) for 1 hour at
686 room temperature and DAPI stain for 5 minutes. Fluorescence image was taken on microscope
687 (DMi8, Leica Biosystems) using Leica Application Suite X (Leica Biosystems) imaging software,
688 and fraction of YFP+ and RFP+ cells as well as the number of CD3+ cells in each tile were
689 quantified using CellProfiler ver. 3.1.9.
690
691 Overexpression of cytokines and chemokines
692 Mouse *Cx3cl1* gene was amplified using forward primer 5' -aactcgagatggctccctcgccgctcg -3' and
693 reverse primer 5' -ttccgcggtcacactggcaccaggacgta- 3', cDNAs generated from CIT9 cell line and
694 Q5® High-Fidelity DNA polymerase (NEB). MSCV 2.2-IRES-CFP retroviral vector was generated
695 by replacing GFP of MSCV 2.2-IRES-GFP vector (obtained from James Carlyle lab at University of
696 Toronto) with CFP. Using restriction enzymes XhoI and SacII, *Cx3cl1* coding sequencing was
697 cloned into MSCV 2.2-IRES-GFP vector. Proviral vectors Gag/Pol and VSV-G were co-transfected

698 with Cx3cl1-IRES-GFP MSCV2.2 vector using lipofectamine 3000 (Invitrogen) into HEK293T cells.
699 48 hours later, the viruses were collected, mixed with CIT6-YFP cells and spinfected at 800g for
700 90 minutes. YFP^+ CFP^+ transduced cells were sorted 72 hours post-transduction.
701
702 ZipSeq spatial transcriptomics analysis
703 Mixed-population tumors were harvested at 1cm in diameter and sliced into 200µm section in
704 2% agarose using vibratome. Section was incubated with CD45 antibody linked to Cy5-
705 conjugated photocaged oligo for 1 hour at 4C°, followed by patterned illumination of a user-
706 defined region of interest[25] and incubation with a unique ZipCode. The process was repeated
707 for YFP, RFP and mixed regions. The section then was digested in a Collagenase I and IV blend
708 for 30 minutes at room temperature, and sorted for live $Cy5^+$ cells using FACS Aria II. washed in
709 PBS + 0.04% BSA and then encapsulated following 10× Genomics specifications for 3' v3
710 chemistry with target cell number of 8,000.
711 Libraries were sequenced with a target number of 30,000 reads per cell for gene
712 expression and 3,000 reads per cell for ZipCode barcodes on a Illumina NovaSeq. Demultiplexed
713 fastqs were aligned using CellRanger to the mm10 Ensembl 93 reference genome. Count
714 matrices were used to generate Seurat objects in R keeping only cells with at least 200 detected
715 genes and genes found in at least 3 cells. Cells were further filtered based on a minimum 500
716 gene cutoff and maximum 15% mitochondrial reads. ZipCode counts were normalized using
717 centered log ratio transform and then assigned a dominant ZipCode identity (as in [25]). Cells
718 were then passed through SCTransform regressing for percent mitochondrial reads. Following
719 PCA analysis on the top variable genes, the first 18 principal components were used as inputs

720 for UMAP dimensional reduction and clustering via the FindNeighbors and FindClusters
721 commands. For pathway analysis, lists of genes with average Log_2 fold change >1 for each
722 cluster were used as input for GO Biological Process 2021 repository on EnrichR
723 (https://maayanlab.cloud/Enrichr/).
724
725 Cytokine array
726 70-150mg of tumor pieces were chopped into small pieces in RIPA buffer containing proteinase
727 inhibitor (Cell BioLabs) and homogenized using OctoMACS (Miltenyi Biotec). The homogenate
728 was centrifuged at 400g for 5 minutes followed by further centrifugation at 10,000g for 10
729 minutes at 4C°. The supernatant was collected and stored at -80C°. Protein concentration was
730 measured using DC protein assay kit (BioRad). The sample concentrations were normalized
731 prior to the submission for the analysis by Eve Technologies DM-44 mouse Discovery Assay
732 panel.
733
734 *In vitro* T cell suppression co-culture assay
735 CD8 T cells were isolated from the lymph node of naïve mice with unactivated Confetti cassette
736 using EasySep™ Mouse $CD8^+$ T Cell Isolation Kit (StemCell Technologies) and macrophages were
737 sorted from the tumors via FACS sorting. CD8 T cells were labeled with CFSE and co-cultured
738 with the macrophages at varying ratios in the presence of Mouse T-Activator CD3/CD28
739 Dynabeads™ (Gibco) and analyzed for division and T cell activation markers.
740
741 Immune cell abundance analysis for human RNAseq dataset

742 For analysis of human tumors, T cell, macrophage and monocyte scores were based on
743 previously calculated scores using an average expression level of genes that are uniquely
744 expressed in human T cells, macrophages and monocytes[28]. The CD206^{Hi} macrophage score was
745 calculated by identifying a combination of four genes that are uniquely expressed in the
746 CD206^{Hi} macrophage cluster (cluster 3) of our ZipSeq dataset (*Hmox1, Cx3cr1, Folr2 and F13a1*).
747 This score was normalized against the average expression level of four genes (*Ccr2, Mgl2,*
748 *Nr4a2 and Ciita*), which were expressed in other macrophages but were not expressed in the
749 CD206^{Hi} macrophage cluster.
750
751 Statistical analysis
752 Data were analyzed using Prism 9 (GraphPad) with either Student's t-test for experiments with
753 two arms, one-way ANOVA analysis for experiments with one variable and more than 3
754 experiment conditions, or two-way ANOVA for experiments with two variables and more than 3
755 experiment conditions. Statistical tests for spatial analyses (Fig. 3 and 8) were done using
756 Student's t-test. For Kaplan-Meier survival analyses, log-rank test was used. Graphs show mean
757 ± SEM or mean ± SD; *, $p < 0.05$; **, $p < 0.01$; ***, $p < 0.001$.
758
759 **Acknowledgements**
760 This work was supported by the UCSF Program for Breakthrough Biomedical Research (PBBR)
761 Sandler Fellowship, US National Cancer Institute (NCI) grant R21CA264599, the Huntsman
762 Cancer Institute Cancer Center Support Grant P30CA040214, the Parker Institute for Cancer

763 Immunotherapy, the American Cancer Society, and The Cancer League. We thank the UCSF
764 Biological Imaging Development CoLab and UCSF Parnassus Flow CoLab, RRID:SCR_018206.

765

766 **Author Contributions**

767 M.T., L.L., C.L.-S., and M.Q.R. designed the project and experiments. M.T., L.L. and C.L.-S. led all
768 experiments and data analyses. K.H. and M.T. carried out the ZipSeq single cell transcriptomics
769 experiments and analysis, with support from M.K. A.J.C. and B.S. conducted the analysis of
770 human RNAseq and immune archetype datasets. M.T. and M.Q.R. wrote the manuscript, with
771 input from other co-authors. K.K., D.S., K.N., and Z.A. assisted with experiments. L.F. provided
772 guidance to the studies.

773

774 **References**

775 1. Ribas, A. & Wolchok, J. D. Cancer immunotherapy using checkpoint blockade. *Science*
776 **359**, 1350–1355 (2018).
777 2. Chen, D. S. & Mellman, I. Elements of cancer immunity and the cancer-immune set point.
778 *Nature* **541**, 321–330 (2017).
779 3. Das, S. & Johnson, D. B. Immune-related adverse events and anti-tumor efficacy of
780 immune checkpoint inhibitors. *Journal for ImmunoTherapy of Cancer* **7**, 306 (2019).
781 4. Darvin, P., Toor, S. M., Sasidharan Nair, V. & Elkord, E. Immune checkpoint inhibitors:
782 recent progress and potential biomarkers. *Experimental and Molecular Medicine* **50**, 165
783 (2018).
784 5. McGranahan, N. *et al.* Clonal neoantigens elicit T cell immunoreactivity and sensitivity to
785 immune checkpoint blockade. *Science* **351**, 1463–1469 (2016).
786 6. McGranahan, N. & Swanton, C. Clonal Heterogeneity and Tumor Evolution: Past, Present,
787 and the Future. *Cell* **168**, 613–628 (2017).
788 7. Liu, D. *et al.* Integrative molecular and clinical modeling of clinical outcomes to PD1
789 blockade in patients with metastatic melanoma. *Nat Med* **25**, 1916–1927 (2019).
790 8. Gerlinger, M. *et al.* Intratumor Heterogeneity and Branched Evolution Revealed by
791 Multiregion Sequencing. *New England Journal of Medicine* **366**, 883–92 (2012).
792 9. Hu, X. *et al.* Multi-region exome sequencing reveals genomic evolution from
793 preneoplasia to lung adenocarcinoma. *Nat Commun* **10**, 2978 (2019).

794 10. Turajlic, S. *et al.* Deterministic Evolutionary Trajectories Influence Primary Tumor
795 Growth: TRACERx Renal. *Cell* **173**, 595-610.e11 (2018).
796 11. Abduljabbar, K. *et al.* Geospatial immune variability illuminates differential evolution of
797 lung adenocarcinoma. *Nat Med* **26**, 1054–1062 (2020).
798 12. Nirmal, A. J. *et al.* The Spatial Landscape of Progression and Immunoediting in Primary
799 Melanoma at Single-Cell Resolution. *Cancer Discov* **12**, 1518–1541 (2022).
800 13. Mitra, A. *et al.* Spatially resolved analyses link genomic and immune diversity and reveal
801 unfavorable neutrophil activation in melanoma. *Nat Commun* **11**, 1–18 (2020).
802 14. Combes, A. J., Samad, B. & Krummel, M. F. Defining and using immune archetypes to
803 classify and treat cancer. *Nat Rev Cancer* (2023) doi:10.1038/s41568-023-00578-2.
804 15. Li, J. *et al.* Tumor Cell-Intrinsic Factors Underlie Heterogeneity of Immune Cell Infiltration
805 and Response to Immunotherapy. *Immunity* **49**, 178–193.e7 (2018).
806 16. Wolf, Y. *et al.* UVB-Induced Tumor Heterogeneity Diminishes Immune Response in
807 Melanoma. *Cell* **179**, 219–235.e21 (2019).
808 17. Gejman, R. S. *et al.* Rejection of immunogenic tumor clones is limited by clonal fraction.
809 *Elife* **7**, 1–22 (2018).
810 18. Wong, C. E. *et al.* Inflammation and Hras signaling control epithelial-mesenchymal
811 transition during skin tumor progression. *Genes Dev* **27**, 670–82 (2013).
812 19. Reeves, M. Q., Kandyba, E., Harris, S., del Rosario, R. & Balmain, A. Multicolour lineage
813 tracing reveals clonal dynamics of squamous carcinoma evolution from initiation to
814 metastasis. *Nat Cell Biol* **20**, 699–709 (2018).
815 20. McCreery, M. Q. *et al.* Evolution of metastasis revealed by mutational landscapes of
816 chemically induced skin cancers. *Nat Med* **21**, 1514–1520 (2015).
817 21. Nassar, D., Latil, M., Boeckx, B., Lambrechts, D. & Blanpain, C. Genomic landscape of
818 carcinogen-induced and genetically induced mouse skin squamous cell carcinoma. *Nat*
819 *Med* **21**, 946–954 (2015).
820 22. Snippert, H. J. *et al.* Intestinal Crypt Homeostasis Results from Neutral Competition
821 between Symmetrically Dividing Lgr5 Stem Cells. *Cell* **143**, 134–144 (2010).
822 23. Mehta, A. K., Kadel, S., Townsend, M. G., Oliwa, M. & Guerriero, J. L. Macrophage Biology
823 and Mechanisms of Immune Suppression in Breast Cancer. *Frontiers in Immunology* **12**,
824 643771 (2021).
825 24. DeNardo, D. G. & Ruffell, B. Macrophages as regulators of tumour immunity and
826 immunotherapy. *Nat Rev Immunology* **19**, 369–382 (2019).
827 25. Hu, K. H. *et al.* ZipSeq: barcoding for real-time mapping of single cell transcriptomes. *Nat*
828 *Methods* **17**, 833–843 (2020).
829 26. Korbecki, J. *et al.* Fractalkine/Cx3cl1 in neoplastic processes. *International Journal of*
830 *Molecular Sciences* **21**, 3723 (2020).
831 27. Conroy, M. J. & Lysaght, J. CX3CL1 Signaling in the Tumor Microenvironment. *Adv Exp*
832 *Med Biol* **1231**, 1–12 (2020).
833 28. Combes, A. J. *et al.* Discovering dominant tumor immune archetypes in a pan-cancer
834 census. *Cell* **185**, 184–203.e19 (2022).
835 29. Ishida, Y. *et al.* Pivotal Involvement of the CX3CL1-CX3CR1 Axis for the Recruitment of M2
836 Tumor-Associated Macrophages in Skin Carcinogenesis. *Journal of Investigative*
837 *Dermatology* **140**, 1951–1961.e6 (2020).

838 30. Reed, J. R. *et al.* Fibroblast Growth Factor Receptor 1 Activation in Mammary Tumor Cells
839 Promotes Macrophage Recruitment in a CX3CL1-Dependent Manner. *PLoS One* **7**, e45877
840 (2012).
841 31. Miheecheva, N. *et al.* Multiregional single-cell proteogenomic analysis of ccRCC reveals
842 cytokine drivers of intratumor spatial heterogeneity. *Cell Rep* **40**, 111180 (2022).
843 32. Pelka, K. *et al.* Spatially organized multicellular immune hubs in human colorectal cancer.
844 *Cell* **184**, 4734-4752.e20 (2021).
845 33. Ke, J.-Y. *et al.* Antitumor immune activity by chemokine CX3CL1 in an orthotopic
846 implantation of lung cancer model in vivo. *Mol Clin Oncol* **1**, 35–40 (2013).
847 34. Liu, J. *et al.* Increased CX3CL1 mRNA expression level is a positive prognostic factor in
848 patients with lung adenocarcinoma. *Oncol Lett* **17**, 4877–4890 (2019).
849 35. Gerlach, C. *et al.* The Chemokine Receptor CX3CR1 Defines Three Antigen-Experienced
850 CD8 T Cell Subsets with Distinct Roles in Immune Surveillance and Homeostasis.
851 *Immunity* **45**, 1270–1284 (2016).
852

Figure 1

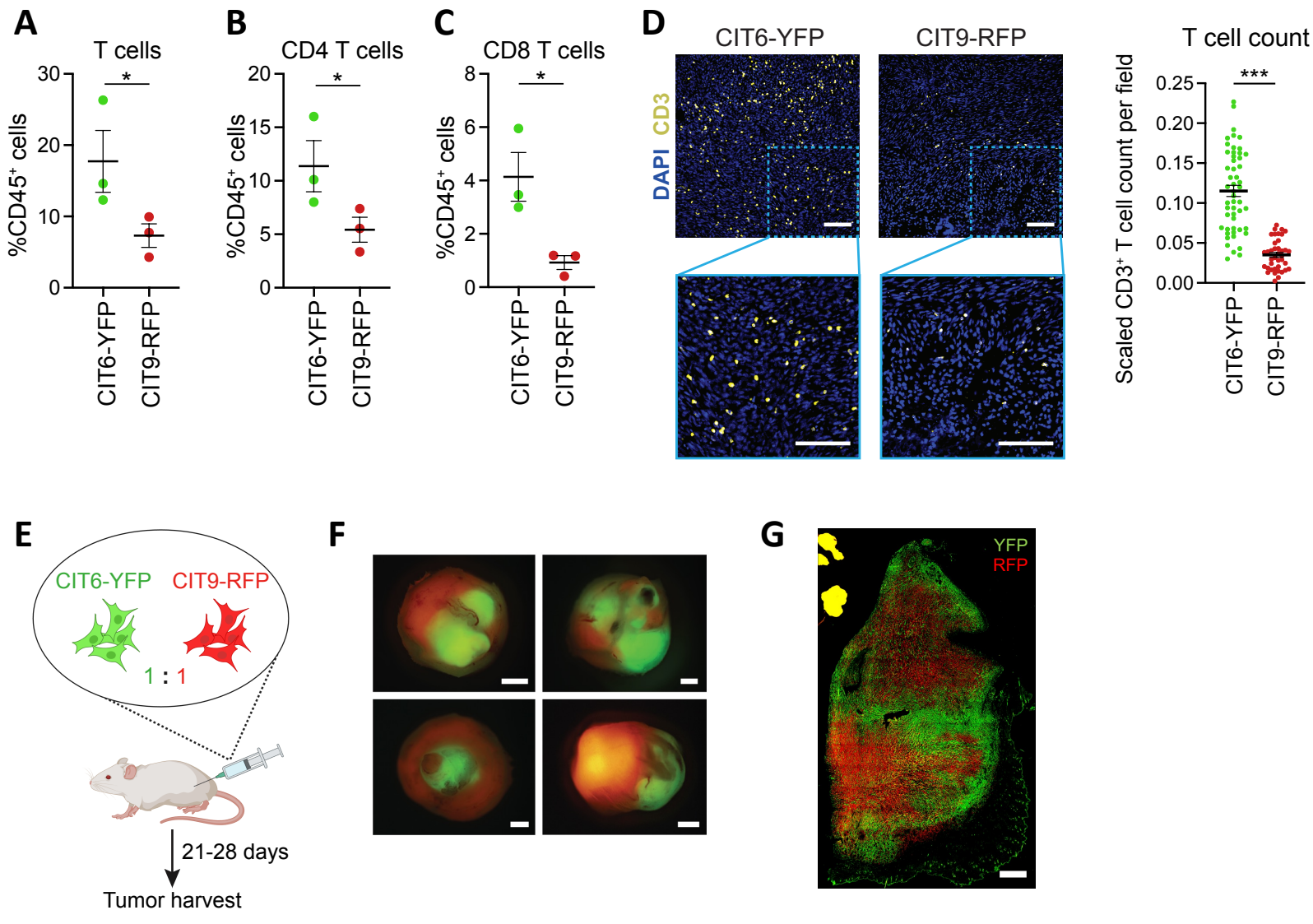
A
T cells
%CD45⁺ cells
30
20
10
0
*
CIT6-YFP
CIT9-RFP
B
CD4 T cells
%CD45⁺ cells
20
15
10
5
0
*
CIT6-YFP
CIT9-RFP
C
CD8 T cells
%CD45⁺ cells
8
6
4
2
0
*
CIT6-YFP
CIT9-RFP
D
CIT6-YFP
CIT9-RFP
DAPI CD3
T cell count
Scaled CD3⁺ T cell count per field
0.25
0.20
0.15
0.10
0.05
0.00
***
CIT6-YFP
CIT9-RFP
E
CIT6-YFP
CIT9-RFP
1 : 1
21-28 days
Tumor harvest
F
G
YFP
RFP

Figure 2

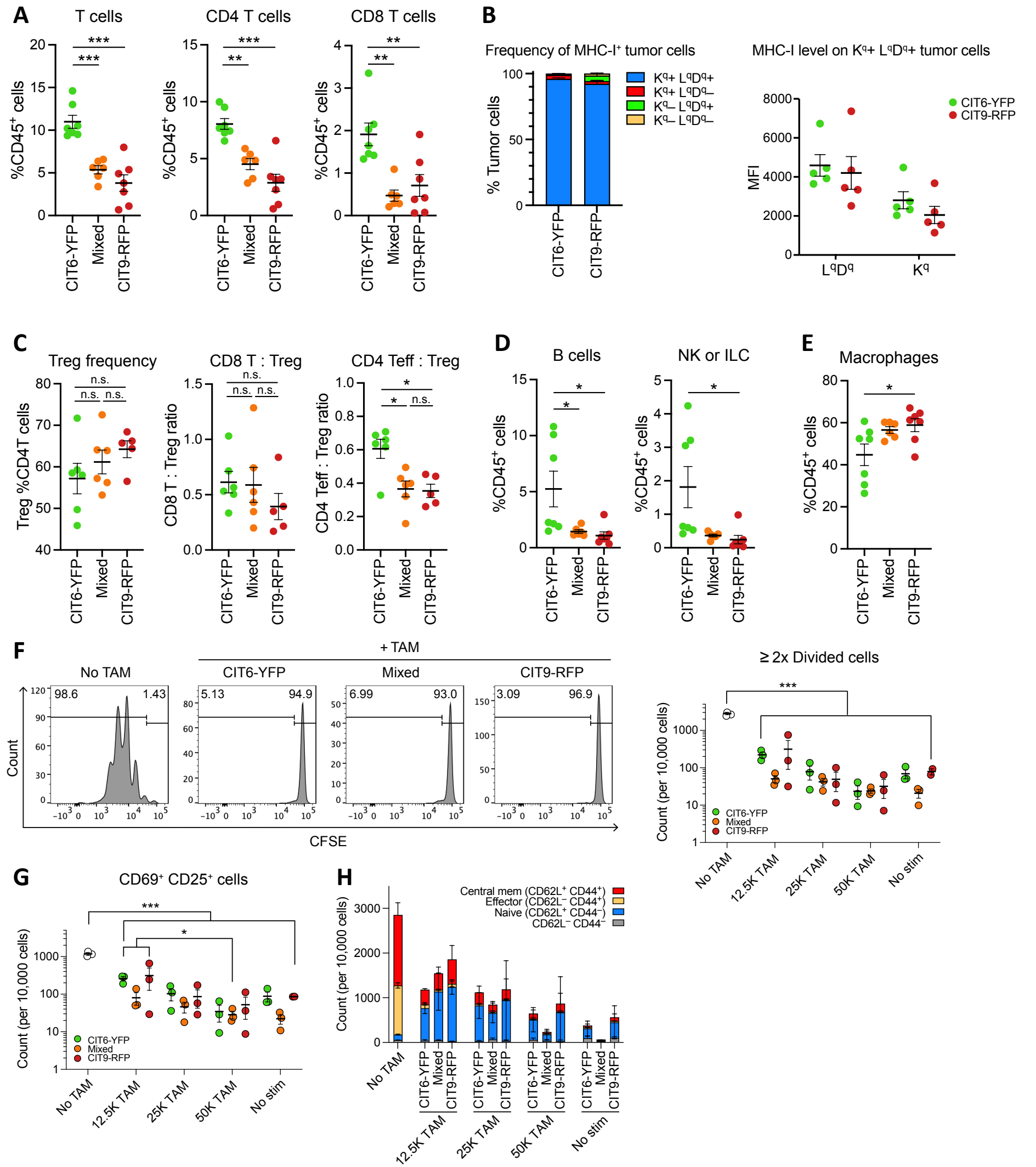
A
T cells
CD4 T cells
CD8 T cells
%CD45+ cells
CIT6-YFP
Mixed
CIT9-RFP
B
Frequency of MHC-I+ tumor cells
% Tumor cells
Kq+ LqDq+
Kq+ LqDq–
Kq– LqDq+
Kq– LqDq–
MHC-I level on Kq+ LqDq+ tumor cells
MFI
LqDq
Kq
C
Treg frequency
CD8 T : Treg
CD4 Teff : Treg
Treg %CD4T cells
CD8 T : Treg ratio
CD4 Teff : Treg ratio
n.s.
D
B cells
NK or ILC
E
Macrophages
F
+ TAM
No TAM
CIT6-YFP
Mixed
CIT9-RFP
98.6
1.43
5.13
94.9
6.99
93.0
3.09
96.9
Count
CFSE
≥ 2x Divided cells
Count (per 10,000 cells)
No TAM
12.5K TAM
25K TAM
50K TAM
No stim
G
CD69+ CD25+ cells
H
Central mem (CD62L+ CD44+)
Effector (CD62L– CD44+)
Naive (CD62L+ CD44–)
CD62L– CD44–

Figure 3

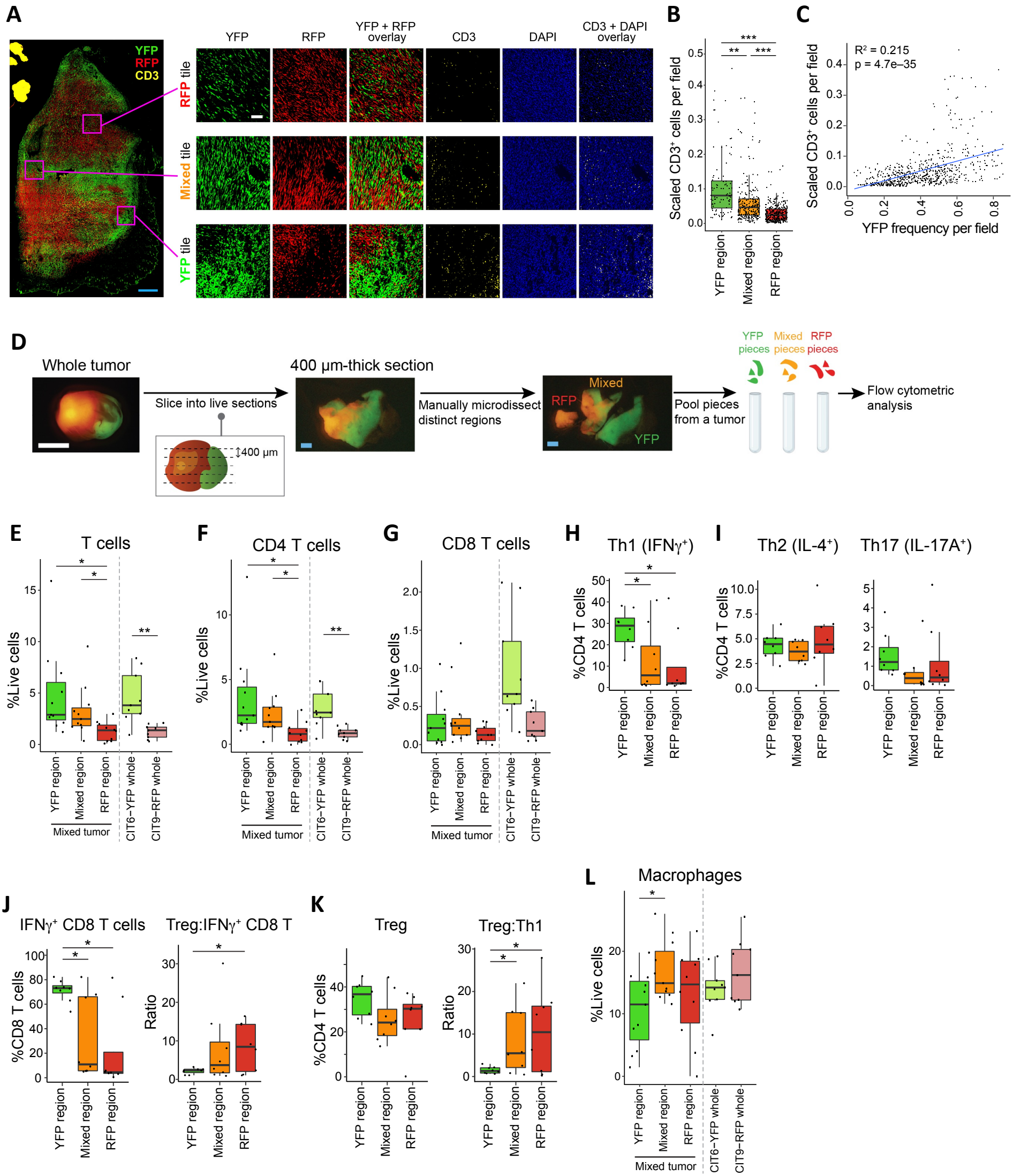
A
YFP
RFP
CD3
YFP
RFP
YFP + RFP overlay
CD3
DAPI
CD3 + DAPI overlay
RFP tile
Mixed tile
YFP tile
B
Scaled CD3⁺ cells per field
YFP region
Mixed region
RFP region
C
R² = 0.215
p = 4.7e–35
Scaled CD3⁺ cells per field
YFP frequency per field
D
Whole tumor
Slice into live sections
400 µm
400 µm-thick section
Manually microdissect distinct regions
Mixed
RFP
YFP
Pool pieces from a tumor
YFP pieces
Mixed pieces
RFP pieces
Flow cytometric analysis
E
T cells
%Live cells
Mixed tumor
CIT6–YFP whole
CIT9–RFP whole
F
CD4 T cells
G
CD8 T cells
H
Th1 (IFNγ⁺)
%CD4 T cells
I
Th2 (IL-4⁺)
Th17 (IL-17A⁺)
J
IFNγ⁺ CD8 T cells
%CD8 T cells
Treg:IFNγ⁺ CD8 T
Ratio
K
Treg
Treg:Th1
L
Macrophages

Figure 4

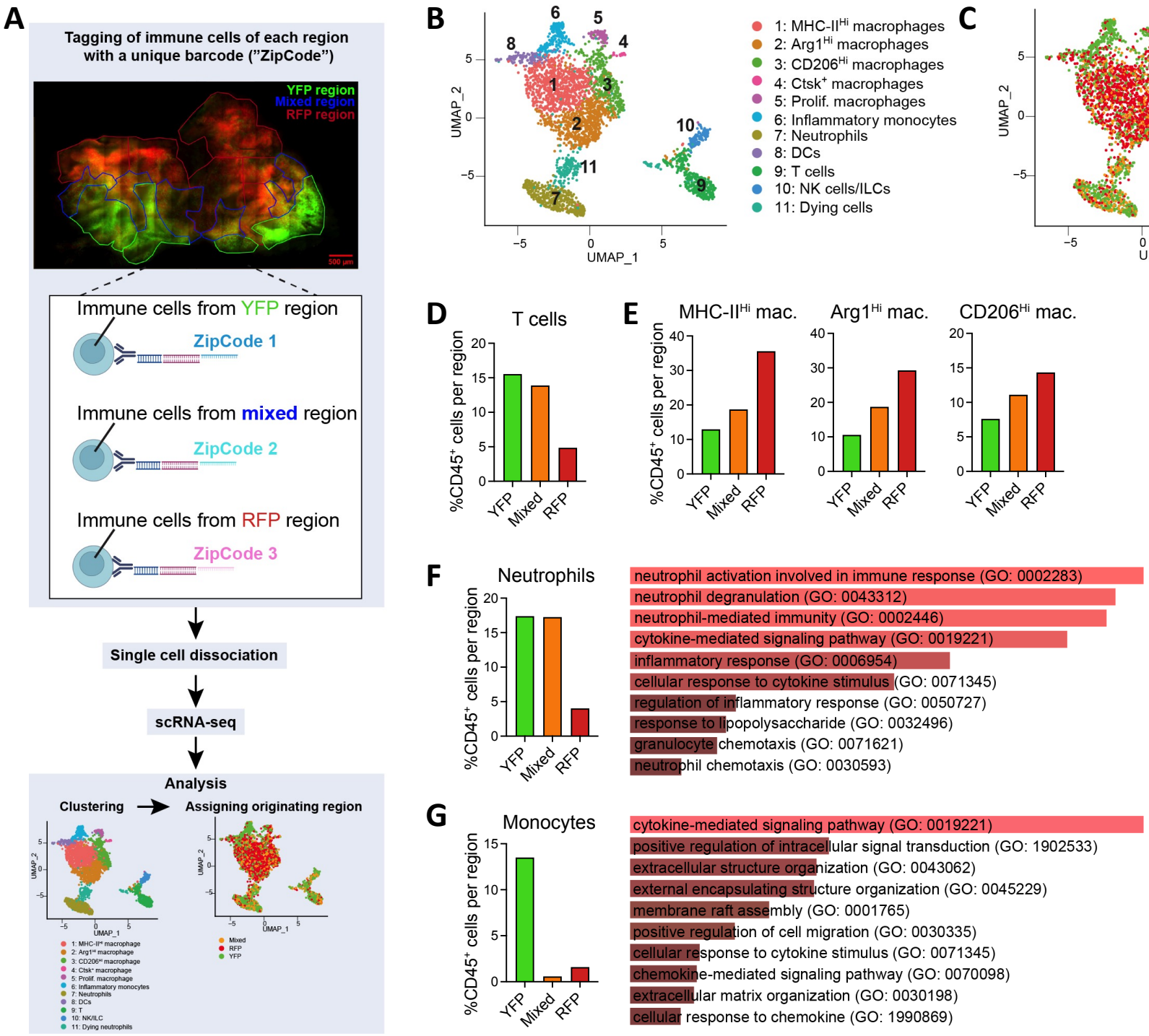
A
Tagging of immune cells of each region with a unique barcode ("ZipCode")
YFP region
Mixed region
RFP region
Immune cells from YFP region
ZipCode 1
Immune cells from mixed region
ZipCode 2
Immune cells from RFP region
ZipCode 3
Single cell dissociation
scRNA-seq
Analysis
Clustering
Assigning originating region
B
1: MHC-II^Hi macrophages
2: Arg1^Hi macrophages
3: CD206^Hi macrophages
4: Ctsk^+ macrophages
5: Prolif. macrophages
6: Inflammatory monocytes
7: Neutrophils
8: DCs
9: T cells
10: NK cells/ILCs
11: Dying cells
UMAP_1
UMAP_2
C
Mixed
RFP
YFP
D
T cells
%CD45^+ cells per region
YFP
Mixed
RFP
E
MHC-II^Hi mac.
Arg1^Hi mac.
CD206^Hi mac.
F
Neutrophils
neutrophil activation involved in immune response (GO: 0002283)
neutrophil degranulation (GO: 0043312)
neutrophil-mediated immunity (GO: 0002446)
cytokine-mediated signaling pathway (GO: 0019221)
inflammatory response (GO: 0006954)
cellular response to cytokine stimulus (GO: 0071345)
regulation of inflammatory response (GO: 0050727)
response to lipopolysaccharide (GO: 0032496)
granulocyte chemotaxis (GO: 0071621)
neutrophil chemotaxis (GO: 0030593)
G
Monocytes
cytokine-mediated signaling pathway (GO: 0019221)
positive regulation of intracellular signal transduction (GO: 1902533)
extracellular structure organization (GO: 0043062)
external encapsulating structure organization (GO: 0045229)
membrane raft assembly (GO: 0001765)
positive regulation of cell migration (GO: 0030335)
cellular response to cytokine stimulus (GO: 0071345)
chemokine-mediated signaling pathway (GO: 0070098)
extracellular matrix organization (GO: 0030198)
cellular response to chemokine (GO: 1990869)

Figure 5

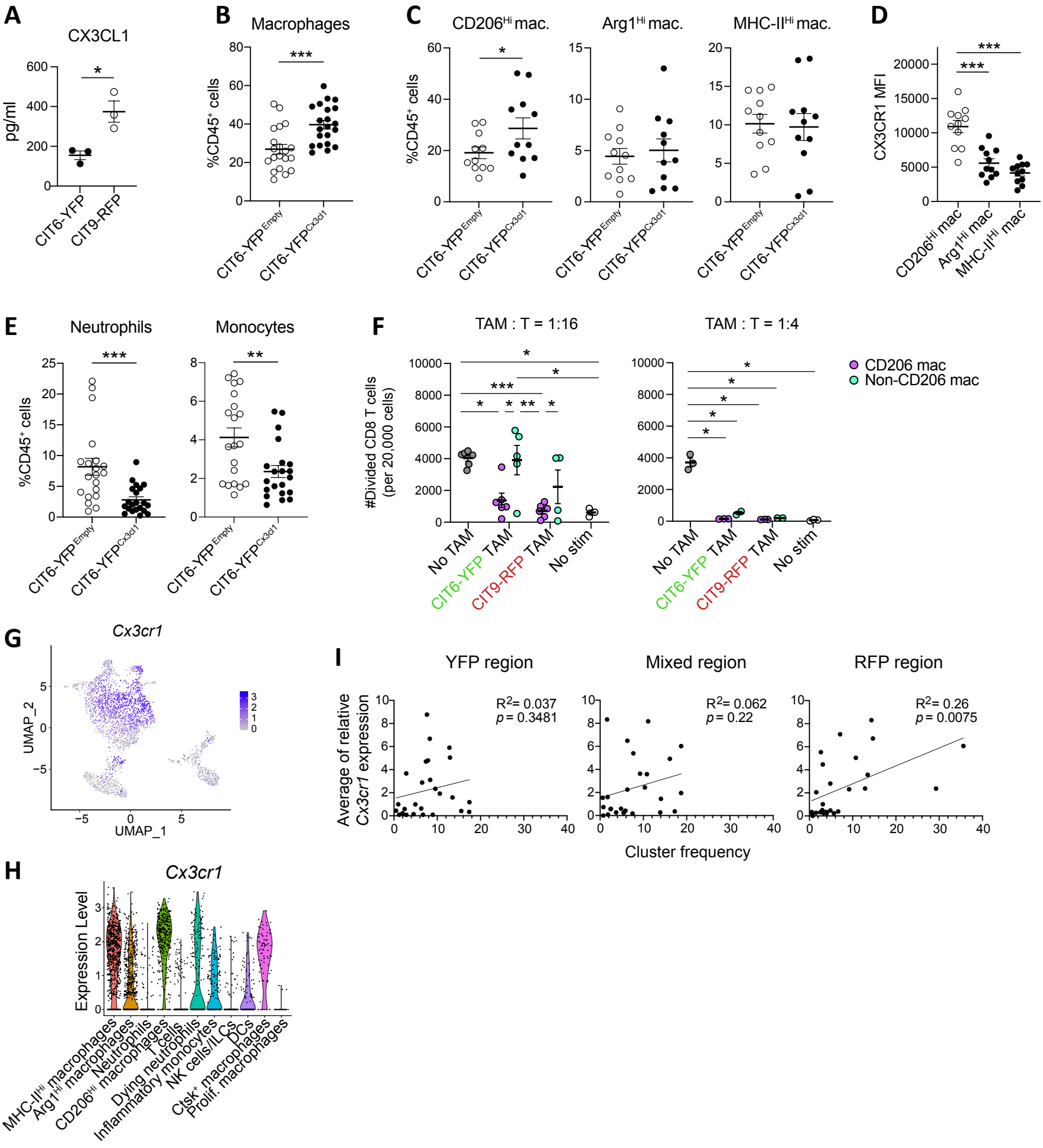
A
CX3CL1
pg/ml
CIT6-YFP
CIT9-RFP
B
Macrophages
%CD45⁺ cells
CIT6-YFP Empty
CIT6-YFP Cx3cr1
C
CD206Hi mac.
Arg1Hi mac.
MHC-IIHi mac.
D
CX3CR1 MFI
CD206Hi mac
Arg1Hi mac
MHC-IIHi mac
E
Neutrophils
Monocytes
F
TAM : T = 1:16
TAM : T = 1:4
#Divided CD8 T cells (per 20,000 cells)
No TAM
CIT6-YFP TAM
CIT9-RFP TAM
No stim
CD206 mac
Non-CD206 mac
G
Cx3cr1
UMAP_1
UMAP_2
I
YFP region
Mixed region
RFP region
Average of relative Cx3cr1 expression
R2= 0.037
p = 0.3481
R2= 0.062
p = 0.22
R2= 0.26
p = 0.0075
Cluster frequency
H
Cx3cr1
Expression Level
MHC-IIHi macrophages
Arg1Hi macrophages
Neutrophils
CD206Hi macrophages
T cells
Dying neutrophils
Inflammatory monocytes
NK cells/ILCs
DCs
Ctsk+ macrophages
Prolif. macrophages

Figure 6

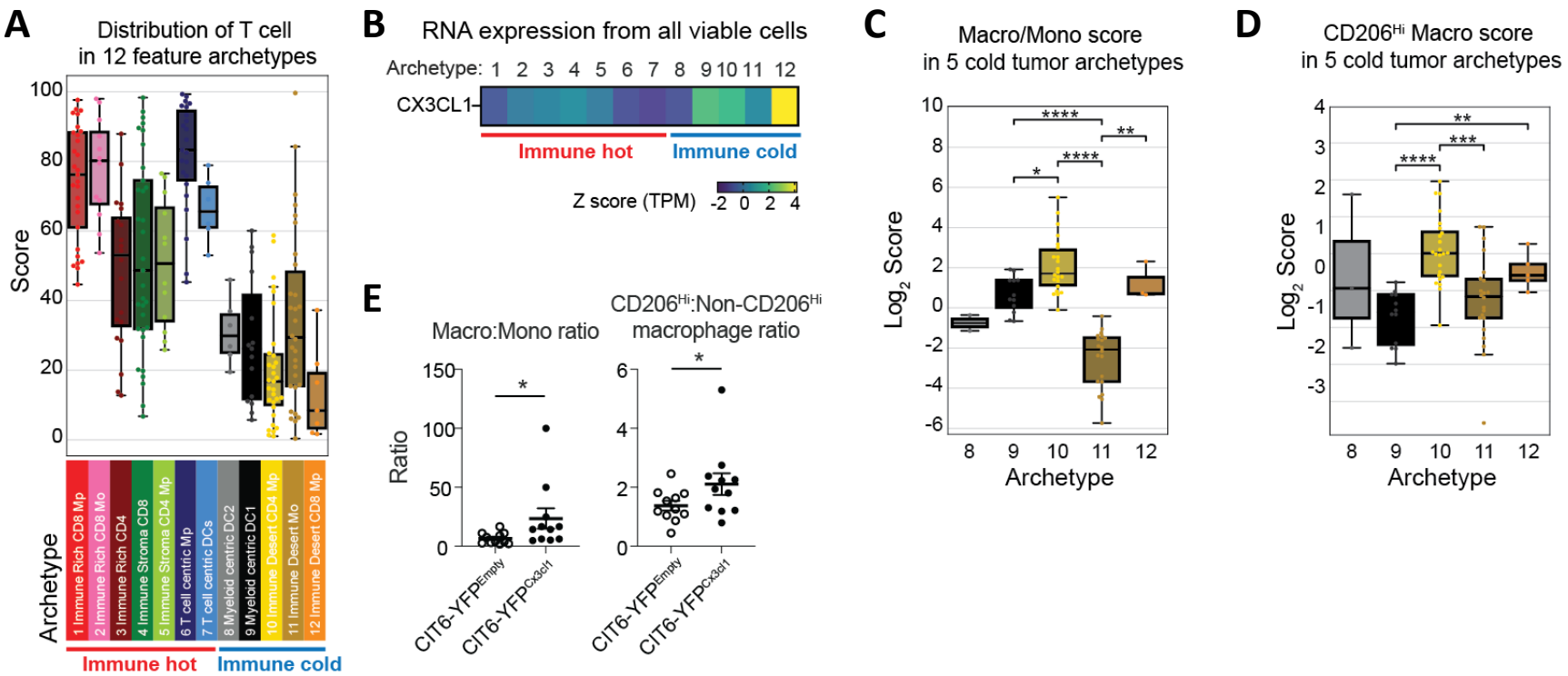
A
Distribution of T cell
in 12 feature archetypes
Score
Archetype
1 Immune Rich CD8 Mp
2 Immune Rich CD8 Mo
3 Immune Rich CD4
4 Immune Stroma CD8
5 Immune Stroma CD4 Mp
6 T cell centric Mp
7 T cell centric DCs
8 Myeloid centric DC2
9 Myeloid centric DC1
10 Immune Desert CD4 Mp
11 Immune Desert Mo
12 Immune Desert CD8 Mp
Immune hot
Immune cold
B
RNA expression from all viable cells
Archetype: 1 2 3 4 5 6 7 8 9 10 11 12
CX3CL1
Immune hot
Immune cold
Z score (TPM) -2 0 2 4
C
Macro/Mono score
in 5 cold tumor archetypes
Log2 Score
Archetype
D
CD206Hi Macro score
in 5 cold tumor archetypes
Log2 Score
Archetype
E
Macro:Mono ratio
CD206Hi:Non-CD206Hi
macrophage ratio
Ratio
CIT6-YFPEmpty
CIT6-YFPCx3cl1

Figure 7

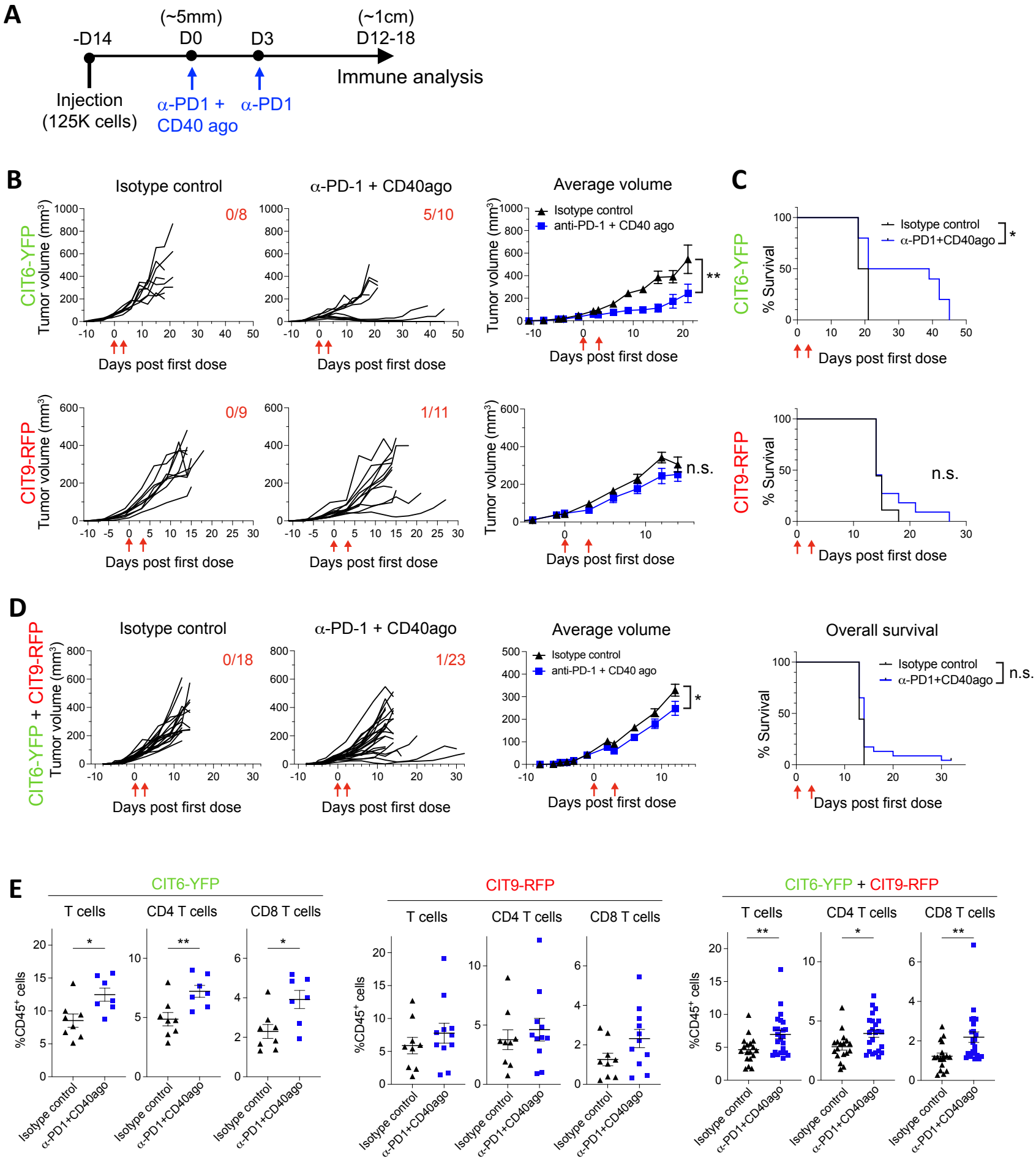
A
-D14
(~5mm)
D0
D3
(~1cm)
D12-18
Immune analysis
Injection
(125K cells)
α-PD1 +
CD40 ago
α-PD1
B
Isotype control
α-PD-1 + CD40ago
Average volume
CIT6-YFP
CIT9-RFP
Tumor volume (mm³)
Days post first dose
0/8
5/10
0/9
1/11
Isotype control
anti-PD-1 + CD40 ago
**
n.s.
C
% Survival
α-PD1+CD40ago
*
n.s.
D
CIT6-YFP + CIT9-RFP
0/18
1/23
Overall survival
E
CIT6-YFP
CIT9-RFP
CIT6-YFP + CIT9-RFP
T cells
CD4 T cells
CD8 T cells
%CD45⁺ cells
Isotype control
α-PD1+CD40ago

Figure 8

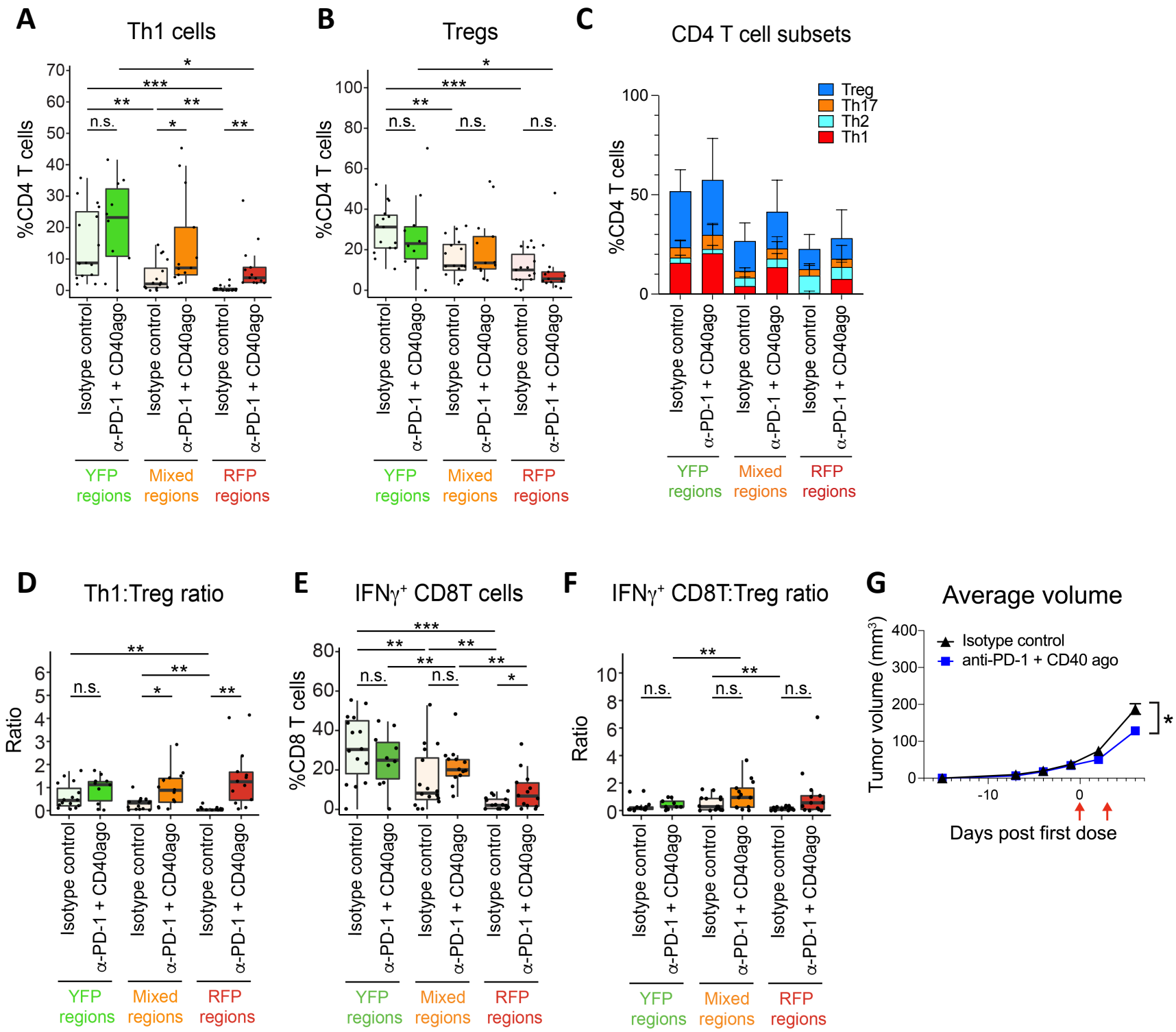
A
Th1 cells
%CD4 T cells
n.s.
*
**
***
Isotype control
α-PD-1 + CD40ago
YFP regions
Mixed regions
RFP regions
B
Tregs
%CD4 T cells
C
CD4 T cell subsets
%CD4 T cells
Treg
Th17
Th2
Th1
D
Th1:Treg ratio
Ratio
E
IFNγ+ CD8T cells
%CD8 T cells
F
IFNγ+ CD8T:Treg ratio
Ratio
G
Average volume
Tumor volume (mm3)
Isotype control
anti-PD-1 + CD40 ago
Days post first dose